

The opposition effect in Saturn's rings seen by

Cassini/ISS:

I. Morphology of phase curves

Estelle Déau ^a, Sébastien Charnoz ^a, Luke Dones ^b,

André Brahic ^a, and Carolyn C. Porco ^c

^a*CEA Saclay DSM/Irfu/SAP AIM UMR 7158, Orme des Merisiers, Bat. 709
91191 Gif-sur-Yvette FRANCE*

^b*Southwest Research Institute, 1050 Walnut Street, Suite 300 Boulder CO 80302,
USA*

^c*CICLOPS, 3100 Marine Street Suite A353, Boulder CO 80303, USA*

Number of pages: 45

Number of tables: 5

Number of figures: 13

Running head: The opposition effect in Saturn's rings seen by Cassini/ISS 1.

Direct editorial correspondence to :

Estelle DÉAU

CEA Saclay

Service d'Astrophysique

AIM, UMR 7158

Orme des Merisiers Bat. 709

91191 Gif-sur-Yvette FRANCE

phone: +33 1 69 08 80 56

fax: +33 1 69 08 65 77

e-mail : estelle.deau@cea.fr

1 **ABSTRACT**

2 The Cassini cameras have captured the opposition effect in Saturn's rings with a high
3 radial resolution at phase angles down to 0.01° in the entire main ring system. We de-
4 rive phase functions from 0.01° to 25° of phase angle in the Wide-Angle Camera clear
5 filters with a central wavelength $\lambda_{cl}=0.611 \mu\text{m}$ and phase functions from 0.001° to 25° of
6 phase angle in the Narrow-Angle and Wide-Angle Cameras color filters (from the blue,
7 $\lambda_{bl}=0.451 \mu\text{m}$ to the near infrared $\lambda_{it}=0.752 \mu\text{m}$). We characterize the morphology of the
8 phase functions of different features in the main rings. We find that the shape of the phase
9 function is accurately represented by a logarithmic model (Bobrov 1970, in Surfaces and
10 Interiors of Planets and Satellites, Academic, edited by A. Dollfus). For practical pur-
11 poses, we also parametrize the phase curves by a simple linear-by-part model (Lumme
12 and Irvine 1976, Astronomical Journal, 81, p865), which provides three morphological
13 parameters : the amplitude and the Half-Width at Half-Maximum (HWHM) of the surge,
14 and the slope S of the linear-part of the phase function at larger phase angles. Our anal-
15 ysis demonstrates that all of these parameters show trends with the optical depth of the
16 rings. These trends imply that the optical depth is a key-element determining the physical
17 properties which act on the opposition effect. Wavelength variations of the morphological
18 parameters of the surge show important trends with the optical depth in the green filter
19 ($\lambda_{gr}=0.568 \mu\text{m}$), which implies that grain size effects are maximum in this wavelength.

20 *Keywords:* Saturn's rings; phase curves; opposition effect; coherent backscattering; shad-
21 owing; shadow hiding

22 1 Introduction

23 When one views the rings of Saturn with the Sun directly behind the observer, a phe-
24 nomenon called the *opposition effect* can be seen. The opposition effect, also known as the
25 opposition surge, is a sudden, nonlinear rise in brightness with decreasing phase (Sun-
26 ring-observer) angle that occurs as the phase angle approaches zero. The opposition
27 effect, which was observed for most Solar System bodies (e.g., Helfenstein et al., 1997;
28 Shkuratov et al., 1999; Belskaya and Shevchenko, 2000; Belskaya et al., 2003; Simonelli and Buratti, 2004;
29 Verbiscer et al., 2005, 2007; Rosenbush et al., 2006) and (Rabinowitz et al., 2007) was dis-
30 covered in the course of Müller’s long-term photometry of the Saturn system, beginning
31 in 1878 (e.g. Müller, 1885, 1893). Seeliger (1884, 1887) inferred that the opposition effect
32 was due to the rings, since Jupiter did not show a comparable opposition brightening
33 (Pollack, 1975).

34 Most recent studies of the opposition effect in the Saturn’s rings were based on ground
35 based and spatial data which resolved the main rings (Lumme and Irvine, 1976; Esposito et al., 1979;
36 Poulet et al., 2002; French et al., 2007). Earth-based observations, though valuable, have
37 a low to moderate spatial resolution (for the Hubble Space Telescope, 1 pixel at Sat-
38 urn =285 km and the full-width at half-maximum (FWHM) of the point-spread func-
39 tion of Hubble’s Camera =7 pixels, see Cuzzi et al., 2002). This indicates that the sig-
40 nal is averaged over large regions in the rings. Unfortunately, the rings are highly het-
41 erogeneous features that may present rapid spatial variations of their optical properties
42 (Esposito et al., 1987). So the interest of *spacecraft* observations is the ability to probe
43 the signal in very narrow ring features (~ 40 km in the present paper), which may have
44 much more uniform optical properties. This allows an easier study of the opposition effect
45 which is an already complex phenomenon.

46 Pioneer 11, Voyager 1 and Voyager 2 did not observe the rings at phase angles near
47 zero. However, Cassini, which became an artificial satellite of Saturn in 2004, is the

48 first spacecraft to observe the opposition effect in the rings, with several instruments
49 (Nelson et al., 2006; Altobelli et al., 2007), including the Narrow Angle (NAC) and Wide
50 Angle (WAC) cameras of the Imaging Science Subsystem (ISS). For our data set (Ta-
51 ble 1), typically for the WAC 1 pixel=40 km and the FWHM is 1.8 pixels, for the NAC
52 1 pixel=5 km and the FWHM is 1.3 pixels (Porco et al., 2004). With Cassini images we
53 are thus able to characterize how the surge varies throughout individual features in the
54 ring system.

55 The opposition effect is now known to be the combined effect of the coherent backscat-
56 ter (at small phase angles) which is a constructive interference of photons in a medium
57 of using grains of wavelength size and the shadow hiding (at larger phase angles) which
58 consists of shadows cast by particles on other particles that become invisible to the ob-
59 server (Helfenstein et al., 1997). Some analytical models have tried to combined these
60 two effects (Shkuratov et al., 1999; Hapke, 2002), but recent laboratory measurements
61 and data analysis show that models' results could be compromised by some physical as-
62 sumptions on the scatterer elements, the wavelength-dependence and the the angular size
63 of the source (Shepard and Helfenstein, 2007; Shkuratov et al., 2007; Déau et al., 2008).
64 Two other effects, the external near-field effect and the single scattering internal-field
65 coherence, were never been observed solely because they are intrinsically inseparable
66 from the coherent backscatter effect and are for the moment only numerically simulated
67 (Petrova et al., 2007; Muinonen et al., 2007).

68 Both shadow-hiding and coherent backscattering are likely to play roles in determining the
69 shape of the phase curves of Solar System bodies at low phase angles (Helfenstein et al., 1997;
70 Hapke et al., 1998). Shadow-hiding probably dominates at phase angles greater than a few
71 degrees, while coherent backscattering takes effect at the very smallest phase angles. The
72 shadow-hiding effect gives clues about the three-dimensional structure of a layer of ring
73 particles which, according to Kawata and Irvine (1974), could have a typical size of $\bar{r} =$
74 15m (see also Salo and Karjalainen, 2003; French et al., 2007). By contrast, the coherent

75 backscattering component sheds light on the nature of the ring particle surfaces at a scale
76 not much larger than optical wavelengths. Indeed, previous photometric studies which
77 investigate the opposition effect in the Saturn's rings determined ranges of typical size
78 for coherent-backscattering effect of about $d = 10 \mu\text{m}$ (Mishchenko and Dlugach, 1992a;
79 Poulet et al., 2002; French et al., 2007). Thus, the shape of the opposition effect provides
80 constraints on features vastly smaller than the camera's resolution.

81 Like Poulet et al. (2002), we refer to particles as macroscopic and individual objects in
82 the rings and grains as microscopic objects at the surface of rings' particles. Using this
83 terminology, ring particles might be covered by regolithic grains.

84 This is the first of a series of papers dealing with the opposition effect in Saturn's rings as
85 seen by ISS/Cassini. In the present paper, we focus on the characterization of the morpho-
86 logical modeling of the shape of opposition effect in the rings. Since the recent theories
87 have difficulties to link the behavior of the opposition effect with the physical proper-
88 ties of the surface material (Nelson et al., 2000; Shepard and Helfenstein, 2007), we think
89 it is necessary to have an experimental approach, consisting in (1) deriving the shape's
90 parameters and (2) trying to find correlations among themselves, and with the optical
91 depth. In the second paper (Déau et al. in preparation), we will use recent analytical
92 photometric models to derive some of the physical properties of the ring material. Indeed,
93 to constrain completely the physical properties of the ring material, photometric and po-
94 larimetric phase curves are needed, however, Cassi/ISS did not captured the opposition
95 spot with its polarized filters.

96 In section 2 of the present paper, we describe the ISS/Cassini data set and our procedure
97 for extracting photometric data from images and fitting empirical models to the data. In
98 section 3, we characterize the morphology of the opposition surge at different locations in
99 the main rings and focus our attention on cross-correlations among the morphological pa-
100 rameters and correlations of these parameters with the optical depth and the wavelength.
101 Finally, in section 4 we discuss these results and examine to which extents photometric

102 models may explain the morphological trends derived in section 2.

103 **2 Observations and reductions**

104 *2.1 The Cassini Imaging Data Set*

105 The Cassini ISS instrument is composed of two cameras, a wide angle camera (WAC) and
106 a narrow angle camera (NAC) equipped with 1024×1024 CCD matrices. Both use a set
107 of about twenty filters ranging from near-infrared to ultraviolet (Porco et al., 2004).
108 Here, we focus only on filters in the optical domain, with first the blue, green, red and near
109 infrared filters, that will be called hereafter COLOR filters. According to (Porco et al., 2004),
110 COLOR filters from NAC and WAC cameras do not have exactly the same central
111 wavelength. For the blue filters, the NAC can have two different combinations of fil-
112 ters (CL1,BL1) or (BL1,CL2) which lead to two central wavelengths : $\lambda_{\text{bl}}^{\text{NAC}} = 0.440\mu\text{m}$
113 and $\lambda_{\text{bl}}^{\text{NAC}} = 0.451\mu\text{m}$. In contrast, for the WAC, the blue (CL1,BL1) filter is charac-
114 terized by a wavelength of about $\lambda_{\text{bl}}^{\text{WAC}} = 0.460\mu\text{m}$. Because the spectral width of these
115 filters is about $\pm 0.050\mu\text{m}$, we consider all images from blue filters of the NAC and the
116 WAC as a consistent whole. The green filter (CL1,GRN) has almost the same spectral
117 characteristics for the two cameras since the central wavelength of $\lambda_{\text{grn}}^{\text{NAC}} = 0.568\mu\text{m}$ for
118 the NAC and $\lambda_{\text{grn}}^{\text{WAC}} = 0.567\mu\text{m}$ for the WAC. The red filter for the NAC corresponds to
119 the filter (RED,CL2) with a central wavelength of $\lambda_{\text{red}}^{\text{NAC}} = 0.650\mu\text{m}$. For the WAC, the
120 combination (CL1,RED) is at a central wavelength of $\lambda_{\text{red}}^{\text{WAC}} = 0.649\mu\text{m}$, which does not
121 change to the that of the NAC at one nanometer. Finally, the filter (CL1,IR1) in the
122 near infrared shows a difference of 10 nanometers between the central wavelength of the
123 NAC ($\lambda_{\text{ir}}^{\text{NAC}} = 0.752\mu\text{m}$) and that of the WAC ($\lambda_{\text{ir}}^{\text{WAC}} = 0.742\mu\text{m}$). In summary, with this
124 moderately high spectral resolution, the combination of images that are not coming ex-
125 actly from the same filters are responsible for a shift of the central wavelength from 0.001

126 to 0.010 micron. Because each filter has a non negligible spectral range ($\pm 0.050\mu\text{m}$), we
127 consider without distinction the COLOR filters from the NAC and WAC cameras and in
128 the rest of the paper, we take as a reference the following wavelengths ($\lambda_{\text{bl}} = 0.451\mu\text{m}$;
129 $\lambda_{\text{grn}} = 0.568\mu\text{m}$; $\lambda_{\text{red}} = 0.650\mu\text{m}$ and $\lambda_{\text{ir}} = 0.752\mu\text{m}$) to designate each COLOR phase
130 curve.

131 The other part of images discussed in the present paper has been taken in CLEAR mode
132 of the WAC, designating the absence of filters resulting in a spectral bandwidth spanning
133 from 0.20 to 1.10 μm (the central wavelength is $\lambda_{\text{cl}} = 0.611\mu\text{m}$ and the spectral range is
134 $\pm 0.450\mu\text{m}$).

135 For the present paper, the selected observation campaign of the opposition effect on the
136 Saturn's rings is divided in four sequences from May 2005 to July 2006 (Table 1).

137 **[Table 1]**

138 These observations were conducted conjointly by the VIMS, CIRS and ISS instruments.
139 Three of ISS sequences were obtained using the WAC only and the last one using the
140 BOTSIM mode (using both cameras simultaneously). Depending on the sequence, different
141 filters were used and different spatial and angular resolutions were achieved. In the present
142 paper, the first of a series aimed at a detailed study of the opposition effect, we will focus
143 on sequences obtained using the WAC camera in CLEAR filter mode and sequences using
144 NAC and WAC cameras in COLOR filter mode, Table 1. Images of the B and C ring are
145 shown in Fig. 1 and 2 to illustrate the quality of the data set.

146 **[Fig. 1, Fig. 2]**

147 In the CLEAR filter mode, the wide angle camera captured rings at zero phase angle two
148 times in 2005, on June 7 and June 26 (they will be designated as *June 7* and *June 26*
149 sequences in the rest of the paper, for practical purpose).

150 In the *June 7* sequence, the WAC images have an average resolution of ~ 44 km per
151 pixel; the rings are observed in reflexion. In each individual image, the phase angle varies

152 by about 3 degrees. In the majority of the set, the opposition point at zero phase an-
153 gle is visible with a very good sampling : about 0.005 degree per pixel. This set covers
154 the full ring system by tracking the opposition spot. Most of the set has an excellent
155 photometric quality, however in dark regions the strong Saturnshine produces ghost im-
156 ages of the secondary mirror perturbing the signal significantly. The amplitude of this
157 artifact is quite constant, about 0.05 in I/F (I/F is the phase-corrected reflectivity, see
158 Porco et al., 2004), which does not significantly affect the photometry of the bright re-
159 gions as A and B rings. However it is very troublesome for dark regions like the D ring, the
160 C ring and the Cassini Division. This is why images from the *June 7* sequence have not
161 been considered for these two regions. The same instrument artifact has been observed
162 and discussed in (Hedman et al., 2007a).

163 The *June 26* sequence has similar characteristics, see Table 1, with a better radial reso-
164 lution of about 30 km per pixel and spans the B and C rings. The presence of the ghost
165 signal in the C ring is not clear. A detailed photometric analysis in these images (cf.
166 section 3.1.1) shows that the derived phase function is consistent with an unperturbed
167 signal, very differently from images in which the ghost were clearly identified. It is why
168 the images of the C ring taken on *June 26* have been considered for the C ring phase
169 function.

170 The *July 23* sequence has the best radial resolution ($\sim 13 \text{ km.pixel}^{-1}$) and spans all A, B,
171 C rings and the Cassini Division (the radial location of the opposition spot in each image
172 is represented in the Fig. 3). In this set, the ghost artifact is absent owing to a much larger
173 angular separation with the bright Saturn globe. Some images of this sequence provide
174 also the larger phase angles.

175 **[Fig. 3]**

176 In COLOR filters mode, the ISS instrument uses the BOTSIM mode in the *May 20*
177 sequence, using both cameras simultaneously for a ride in A and B rings, Cassini Division
178 and the outer C ring (Fig. 3). However, because the boresight of the NAC and the NAC

179 are not exactly the same, NAC images did not represent a zoom of the opposition spot in
180 WAC images. Thus, WAC and NAC images captured at the same time have opposition
181 spots that are not exactly at the same location in the rings. The radial resolution in NAC
182 images is $4.6 \text{ km}\cdot\text{pixel}^{-1}$ and spans from 44 to $66 \text{ km}\cdot\text{pixel}^{-1}$ for WAC images in COLOR
183 filters. The other sequences (*Dec 31, Feb 20* and *Apr 25*), did not have the opposition
184 spot but provided the larger phase angles.

185 *2.2 Data reduction*

186 *2.2.1 Calibration*

187 Raw images are calibrated first with a standard pipeline described in (Porco et al., 2004)
188 and called CISSCAL, using the 3.4 version. The DN values are converted into the I/F
189 units. This ratio is dimensionless, with I is the specific intensity measured by Cassini, and
190 πF is the incident flux from the Sun. So it is a measure of the local reflectivity under the
191 current observing geometry.

192 Cassini images are not directly exploitable to study the photometric behavior of rings.
193 In order to do this, the relevant data we need are the so-called *phase function* which
194 is linked to the I/F ratio as a function of the phase angle, and corrected from effects
195 of observation geometry. A full procedure has been designed to reconstruct the phase
196 function from different images with different observation geometry and resolutions and is
197 detailed below.

198 *2.2.2 Extraction procedure*

199 The first step is to reproject the images in a (Radius, Longitude) frame, in which features
200 at a same radius from Saturn are horizontally aligned. This procedure critically depends
201 on the quality on the navigation. When possible, the edges of the A, B, C rings as well as
202 ring features reported in (Esposito et al., 1987) were used as fiducial references. Distances

203 reported in (Esposito et al., 1987) were corrected according to (Nicholson et al., 1990).
204 The resulting navigation error on WAC images varies from 1 to 1.5 pixels from the center
205 to the edge of the image.

206 The I/F in a ring at constant distance from Saturn is obtained by extracting the data
207 on a line of constant radius (*i.e.* an horizontal line) in the reprojected map of calibrated
208 brightness. Other geometrical parameters are extracted in the same way : phase angle α ,
209 cosine of incidence angle μ_0 , cosine of the emission angle μ , optical depth of the rings ob-
210 tained from the PPS Voyager instrument ($\lambda = 0.260 \mu\text{m}$), (Esposito et al., 1987); radius
211 scale has been corrected with the procedure of Nicholson et al. (1990).

212 This procedure works very well for structures with width larger than the navigation ac-
213 curacy. However radial structures are visible at all scales down to one pixel, (Fig. 2). For
214 structures radially smaller than 5 pixels, navigation errors make false the extraction along
215 a line of constant radius close to the edges of the image, inducing accidental extraction
216 in nearby different features. To overcome this problem and to ensure that we always ex-
217 tract the same ring feature, we developed a *ring tracking* technique using a basic pattern
218 recognition algorithm to follow a single feature. Extensive visual check of the result shows
219 the method is reliable down to 1 pixel of radial width.

220 2.2.3 Construction of the phase function

221 The ultimate information we need is the phase function of individual ring particles to
222 characterize their surface properties. Unfortunately, the signal from an individual particle
223 is heavily altered because of the finite thickness of the rings (Porco et al., 2007). Also, the
224 signal's intensity depends on observation angle with respect to the ring's normal. Inverting
225 such complex collective photometric effects would require the use a detailed light scattering
226 code with many assumptions concerning the photometric properties of particles. Such code
227 has been developed by Salo (1992, 1995); Richardson (1994); Porco et al. (1999, 2007)
228 and French et al. (2007). However, for our present purposes, they cannot used to de-

229 rive the phase functions in hundreds of different regions as we wish to do here. Conse-
 230 quently, as a first approximation, we use in the present paper the classical approach of
 231 Chandrasekhar (1960) linking the I/F to the phase function with the following assump-
 232 tions : homogeneous layer of particles and single scattering. This latter assumption may be
 233 justified for phase angles smaller than $\sim 30^\circ$ (Cuzzi et al., 2002). In reflexion, the phase
 234 function $\varpi_0 \cdot P(\alpha)$ is derived from the solution to the radiative transfer equation (the
 235 designation *phase function* is not strictly accurate since what we really determine is the
 236 product of the single scattering albedo, ϖ_0 , times the particle phase function, $P(\alpha)$) :

$$\varpi_0 \cdot P(\alpha) = \frac{I}{F} \times \frac{4(\mu + \mu_0)}{\mu_0} \times \left(1 - e^{-\tau \left(\frac{1}{\mu} + \frac{1}{\mu_0} \right)} \right)^{-1} \quad (1)$$

237 with τ, μ, μ_0, α standing for : the normal optical depth, cosine of emission angle, cosine of
 238 incidence angle and phase angle respectively. In order to allow future comparisons with
 239 detailed numerical models, numerous analytical parametrization of the observations are
 240 provided by morphological model in section 2.3. As one can see, the value of the optical
 241 depth is necessary to derive the phase function. Preceding works has shown that the
 242 exponential factor can be neglected in first approximation for Earth-based observations
 243 (Cuzzi et al., 2002; Poulet et al., 2002). However, we noticed that we obtained much more
 244 coherent results when taking into account the exponential factor, when comparing results
 245 from different geometry of observations. Consequently, we keep the initial formula of
 246 Chandrasekhar (1960), as previous photometric studies based on spacecraft observations
 247 of Saturn's rings (Doyle et al., 1989; Cooke, 1991; Ferrari, 1992; Showalter et al., 1992;
 248 Dones et al., 1993).

249 $P(\alpha)$ obtained with Eq. 1 is the particle's disk integrated phase function which determines
 250 the angular distribution of single scattered radiation from the body as a whole. The
 251 phase function is normalized over the solid angle Ω to the single scattering albedo :
 252 $\varpi_0 = \frac{1}{4\pi} \int P(\alpha) d\Omega$. To derive the albedo, the full phase curve, from 0 to 180 degrees of

253 phase angle, must be known. In this study, we have restricted our data ($0 < \alpha < 25$ degrees),
254 so that we may avoid separating the albedo from the phase function. The derivation of
255 the albedo will be presented in the second paper which relates ISS data from 0 to 180
256 degrees.

257 2.2.4 Finite size of the Sun

258 Generally speaking, all phase curves present a bright opposition surge below 1° and a
259 slope decreasing linearly for $\alpha > 1^\circ$. Whereas WAC images go down to $\sim 0.01^\circ$ of phase
260 angle (Fig. 1), NAC images taken in COLOR filters capture the opposition spot at better
261 angular resolution (Fig. 2), the resulting phase functions from NAC images go down to
262 $\sim 0.001^\circ$ (Fig. 4). This is the first time the opposition spot is imaged at such fine scale.

263 Note that we define the phase angle as the angle between the vector pointing to the Sun's
264 center, and to the spacecraft, from the observed point. So from a strictly *mathematical*
265 *point of view* there is no lower limit to the phase angle value despite the source's finite
266 size. For an extended illumination source, the phase curve should be the integral of a point
267 source phase function over the Sun angular radius. Thus on a more *physical point of view*
268 it is not possible to observe the phase function at angle below the Sun's angular radius
269 (Kawata and Irvine, 1974; Shkuratov, 1991).

270 Fig. 4 demonstrates that the opposition surge flattens (in all rings and at all wavelengths)
271 at phase angles below 0.029° , in good agreement with the Sun's angular radius at the
272 date of observations (0.0291 degree, given by $\alpha_{\odot\min} = \arcsin \frac{r_{\odot}}{R_{\odot-\text{Saturn}}}$ where $r_{\odot} = 6.96 \times$
273 10^5 km is the radius of the Sun and $R_{\odot-\text{Saturn}}$ is the heliocentric distance of Saturn
274 Murray and Dermott, 2000).

275 [Fig. 4]

276 *2.3 Data fit with Morphological models*

277 The purpose of the present paper is to provide an accurate description of the morpho-
278 logical behavior of the observed phase curves. This is the very first step prior to any
279 attempt of further modeling, which will be the subject of a forthcoming paper. As a con-
280 sequence, special care has been given to parametrize the phase functions conveniently. In
281 addition morphological parametrization is necessary to compare efficiently hundreds of
282 phase curves at different locations in the rings and derive statistical trend as will be done
283 in section 3.

284 Several morphological models have been used in the past to describe the shape of the
285 phase functions : the logarithmic model of Bobrov (1970), the linear-by-part model of
286 Lumme and Irvine (1976) and the linear-exponential model of Kaasalainen et al. (2001).
287 The specific properties of these three models make them adapted for different and com-
288plementary purposes. The logarithmic model is interesting for direct comparisons with
289 numerical models, the linear-by-part model is convenient to describe the shape in an in-
290 tuitive way, and finally the linear-exponential model is adapted for comparison with other
291 studies previously published.

292 *2.3.1 The logarithmic model*

293 As Bobrov (1970), Lumme and Irvine (1976) and Esposito et al. (1979), we remark that
294 a logarithmic model describes very well the solar phase curves of the Saturn's rings. It
295 depends on two parameters (a_0 and a_1). This first morphological model has the following
296 form :

$$\varpi_0 P(\alpha) = a_0 + a_1 \times \log(\alpha) \tag{2}$$

297 In general, this model is the best morphological fit to the data. It is reasonably accurate

298 down to 0.029° of phase angle. This is due to the finite angular size of the Sun which
 299 flattens data below 0.029° , whereas the logarithmic function continues increasing (see
 300 section 2.2.4 and Fig. 4a). For large phase angles, the fit is satisfactory up to $\alpha \simeq 15$ degrees,
 301 this was also noticed by Altobelli et al. (2007) who fitted temperature phase curves of the
 302 C ring with CIRS/Cassini.

303 Whereas the meaning of a_0 and a_1 are not easily interpretable in term of shape, to allow
 304 an easy comparison with future numerical simulations the values of these two parameters
 305 are reported in Table 1 of Electronic supplement material.

306 2.3.2 *The linear-exponential model*

307 This model describes the shape of the phase function as a combination of an expo-
 308 nential peak and a linear part. Its main interest is that it has been used in previ-
 309 ous work for the study of the backscattering of Solar System's icy satellites and rings
 310 (Kaasalainen et al., 2001; Poulet et al., 2002; French et al., 2007). We give the details of
 311 this model : the 4 parameters are the intensity of the peak I_p , the intensity of the back-
 312 ground I_b , the absolute slope of the linear part I_s and the width of the exponential w ,
 313 such that the phase function is represented by :

$$\varpi_0 P(\alpha) = I_b + I_s \cdot \alpha + I_p \cdot e^{-\frac{\alpha}{2w}} \quad (3)$$

314 With these 4 parameters, we characterize the shape of the phase function by introducing
 315 three morphological parameters : A, HWHM and S designating the amplitude of the surge,
 316 the half-width at half-maximum of the surge and the absolute slope at large phase angles
 317 respectively, so that :

$$A = \frac{I_p + I_b}{I_b} \quad \text{HWHM} = 2 \cdot \ln 2w \quad \text{and} \quad S = -I_s \quad (4)$$

318 As French et al. (2007), we noticed that this model did not fit well the phase curves, in
 319 particular, the derived model parameters appeared to depend substantially on the phase
 320 angle coverage (see section 2.3.4), preventing a robust comparison of data. This is due to
 321 the fact that we did not use the converging procedure of Kaasalainen et al. (2001) but
 322 rather the common downhill minimization technique, as done by the previous users of
 323 the linear-exponential model (Poulet et al., 2002; French et al., 2007). Moreover, it seems
 324 that the angular scale at which the phase function is observed may strongly influence
 325 the model parameters. So to avoid this problem, we used a much simpler morphological
 326 model that appeared much more robust for the comparison of heterogeneous data set :
 327 the linear-by-part model of Lumme and Irvine (1976), also we found a much better match
 328 of the data with the linear-by-part model of Lumme and Irvine (1976) (see below).
 329 However, the linear-exponential was considered in the present study only to understand
 330 variations of A, HWHM and S between the (Poulet et al., 2002; French et al., 2007) phase
 331 curves and our phase curves (see section 2.3.4 and section 3.2.3).

332 2.3.3 *The linear-by-part model*

333 For an intuitive description of the main features of the phase curves, the linear-by-part
 334 model is the most convenient one. It is constituted of two linear functions fitting both the
 335 surge at small phase angle ($\alpha < \alpha_1$) and the linear regime at higher phase angle ($\alpha > \alpha_2$) :

$$\varpi_0 P(\alpha < \alpha_1) = -A_0 \times \alpha + B_0 \quad \varpi_0 P(\alpha > \alpha_2) = -A_1 \times \alpha + B_1 \quad (5)$$

336 Lumme and Irvine (1976) and Esposito et al. (1979) use $\alpha_1=0.27^\circ$ and $\alpha_2=1.5^\circ$. However,
 337 we encountered difficulties with the value of α_1 . By testing several values of α_1 , it appears
 338 that for our data set, values of α_1 less than 0.3° yield a general overestimation of A_0 ,
 339 especially in the C ring and values of α_1 greater than 0.3° yield an underestimation of
 340 A_0 only in the B ring. Consequently we found the our data were better reproduced using
 341 $\alpha_1 = 0.3^\circ$ which is now adopted in the rest of the paper.

342 With this four outputs : the two absolute slopes A_0 and A_1 and the two y-intercepts B_0 and
 343 B_1 , the shape of the curve is characterized by the morphological parameters A, HWHM
 344 and S are then defined by :

$$A = \frac{B_0}{B_1} \quad \text{HWHM} = \frac{(B_0 - B_1)}{2(A_0 - A_1)} \quad \text{and} \quad S = A_1 \quad (6)$$

345 The purpose of this model is not, of course, an accurate description of the data but rather
 346 a convenient description of the main trends of the phase curve.

347 2.3.4 *Stability of the morphological parameters*

348 In order to compare properly our results with those of Poulet et al. (2002) and French et al. (2007),
 349 for which the Saturn's rings phase curves did not have the same phase angle coverage, we
 350 have tested the influence of the portion 0.05° - 0.4° and 6° - 25° on the converging solution.
 351 Indeed, phase curves of Poulet et al. (2002) do not have data under 0.3° , and both studies
 352 of Poulet et al. (2002) and French et al. (2007) do not have data over 6.5° (the maximum
 353 phase angle reached from Earth is about $\alpha_{\odot\text{max}} = \arcsin \frac{R_{\odot\text{-Earth}}}{R_{\odot\text{-Saturn}}} \lesssim 6.5^\circ$ where $R_{\odot\text{-Earth}}$ is
 354 the heliocentric distance of the Earth and $R_{\odot\text{-Saturn}}$ is the heliocentric distance of Saturn
 355 computed with orbits of Murray and Dermott, 2000).

356 With two typical Saturn's rings phase curves of ISS (Fig. 5), we have removed data by sec-
 357 tion of 0.1° and fit the pseudo-incomplete phase curve with the linear-exponential model,
 358 which provides the new solution, designated by A_{remove} , $\text{HWHM}_{\text{remove}}$ and S_{remove} . The
 359 initial solution found for fuller phase function (0.01° - 25°) is called A_{optimal} , $\text{HWHM}_{\text{optimal}}$
 360 and S_{optimal} . Both solutions are obtained with a downhill minimization technique, to re-
 361 produce the fitting method used by Poulet et al. (2002) and French et al. (2007). It is wise
 362 to recall that Kaasalainen et al. (2001) proposed a converging procedure more accurate,
 363 however because (e.g. Poulet et al., 2002; French et al., 2007) did not used it, and because
 364 we want to reproduce not the best converging solutions but the deviations lead by the fits

365 driven by Poulet et al. (2002) and French et al. (2007), that is why we use the downhill
366 method and not the probability distribution method of Kaasalainen et al. (2001).

367 **[Fig. 5, Fig. 6]**

368 In Fig. 6, we represent the ratio of the morphological parameters of the incomplete phase
369 curve over the morphological parameters of the fuller phase curve, called $A_{\text{remove}}/A_{\text{optimal}}$,
370 $\text{HWHM}_{\text{remove}}/\text{HWHM}_{\text{optimal}}$ and $S_{\text{remove}}/S_{\text{optimal}}$. We observe a slight underestimation of
371 A, a strong overestimation of HWHM and a moderate underestimation of S.

372 The deviation of the optimal value is quite weak for A ($A_{\text{remove}}/A_{\text{optimal}} \sim 0.96$ at a cut-
373 off of 0.3°) but its variation depends on the morphology of the surge. For the typical
374 B ring phase curve (which has a narrower peak), we note a slight decrease of the ratio
375 $A_{\text{remove}}/A_{\text{optimal}}$ and for the C ring, we note a slight increase of the ratio. However the
376 both ratios lead to an underestimation, which means that incomplete data fitted by the
377 morphological model will have a smaller amplitude than data which cover the full surge.
378 HWHM shows the strongest deviation of A_{remove} . Indeed, HWHM is overestimated for
379 the typical B ring phase curve ($\text{HWHM}_{\text{remove}}/\text{HWHM}_{\text{optimal}} \sim 1.4$ at a cutoff of 0.3°) but
380 is strongly overestimated for the typical C ring ($\text{HWHM}_{\text{remove}}/\text{HWHM}_{\text{optimal}} \sim 2.0$ at a
381 cutoff of 0.3°) which has a wider peak.

382 For the slope, we notice an overestimation in the order of $S_{\text{remove}}/S_{\text{optimal}} \sim 1.3$ at a cutoff
383 of 7° for the B ring phase curve and of ~ 2.5 for the C ring at the same cutoff. This means
384 that the slope of the linear part is stabilized at roughly 15° .

385 These comparisons are important when we compare morphological trends found by Poulet et al. (2002),
386 in section 3.1.2 and French et al. (2007), in section 3.2.3.

387 *2.3.5 Linking morphological parameters with the physical parameters of the models*

388 The use of a simple morphological model is generally not adapted to derive the physical
389 properties of the medium. However, the theories developed for the coherent backscatter-

390 ing and the shadow hiding effects deduce their properties by parameterizing the opposition
391 phase curve (Mishchenko and Dlugach, 1992a,b; Mishchenko, 1992; Shkuratov et al., 1999;
392 Hapke, 1986, 2002). Recent laboratory experiments raise some doubts on the meaning of
393 the physical parameters of these models and their correlation with the real physical prop-
394 erties of the medium (Shepard and Helfenstein, 2007; Shkuratov et al., 2007). However,
395 because there is no better modelization, we connect the morphological parameters A ,
396 HWHM and S with the physical characteristics of the medium derived from these models.

397 A is the amplitude of the opposition peak and describes the behavior of the phase func-
398 tion at the smallest phase angles ($\alpha < 2^\circ$). What we know about the opposition ef-
399 fect is that it occurs at the smallest phase angles and acts on the multiple scattered
400 light in the regolith on the surface of the particles : the underlying phenomenon is the
401 coherent backscattering effect. The coherent-backscattering effect increases in bright-
402 ness by almost a factor two, while using grains size smaller than the wavelength of
403 the incident light, (Mishchenko and Dlugach, 1992b; Shkuratov et al., 1999). In con-
404 trast, the second phenomenon of the opposition effect, the shadow hiding effect, is
405 known to produce a wide peak from 0 to 2 degrees, and to decrease the brightness
406 up to 20 degrees (Hapke, 1986; Stankevich et al., 1999). The combination of the two
407 effects at very low phase angle is still a matter of debate and today two theories dis-
408 agree in order to explain the peak of the opposition. The theory of Mishchenko (1992);
409 Mishchenko and Dlugach (1992b) assumes that the opposition peak is a pure coherent
410 backscattering effect whereas the theory of Hapke (2002) shows that the opposition
411 peak results from a coupling of coherent-backscattering and shadow hiding, even at low
412 phase angles. This coupling should be due to the fact that the coherent backscatter-
413 ing could act on both multiple and single scattered light whereas the shadow hiding is
414 a single scattered light effect (Hapke, 2002). Thus, this theoretical model defines two
415 amplitudes as output parameters : the coherent backscatter amplitude B_{C0} and the
416 shadow hiding amplitude B_{S0} . As a consequence, using this theory, it does not seem to

417 be possible to ascribe the morphological parameter A solely to the coherent backscat-
418 tering.

419 For most laboratory measurements (Shkuratov et al., 1999; Nelson et al., 2000), the
420 amplitude of the opposition peak is a function of grain size in such way that A decreases
421 with increasing grain size. This anti-correlation finds a natural explanation by the fact
422 that macroscopic irregularities ($>\lambda$) create less coherent effects than microscopic irreg-
423 ularities ($\leq \lambda$). Laboratory measurements of Kaasalainen (2003) also confirmed that the
424 opposition surge increases when irregularities are small. Mishchenko and Dlugach (1992b)
425 and Mishchenko (1992) underline the fact A is linked to the intensity of the background
426 I_b which is a decreasing function of increasing absorption (Lumme et al., 1990), thus
427 A must increase with increasing absorption or decreasing albedo ϖ_0 , which was also
428 confirmed by laboratory measurements of Kaasalainen (2003) who found that the peak
429 decreases with increasing sample albedo.

430 **HWHM** , the half-width at half-maximum, is generally associated to the coherent backscat-
431 ter effect. It can be related to the grain size, index of refraction and packing density of re-
432 golith (Mishchenko, 1992; Mishchenko and Dlugach, 1992a; Hapke, 2002). The HWHM
433 is maximum for a effective grain size near $\lambda/2$ and increases when the regolith grains fill-
434 ing factor f increases. For high values of f , the HWHM shifts towards the greater grain
435 size. However, as for the amplitude, the model of Hapke (2002) defines two HWHMs :
436 the coherent backscatter angular width (h_c), which is defined similarly that in the model
437 of Mishchenko (1992), and the shadow hiding angular width (h_s). This reinforces the
438 idea that the observed surge results from a coupling between the coherent backscattering
439 and the shadow hiding.

440 **S** , the slope of the linear part, seems to be due only to the shadow hiding effect: the
441 interferences caused by coherent backscattering effect seem not to be very significant
442 at larger phase angles (Mishchenko et al., 2006; Hapke, 2002). This means the shadow
443 hiding light is not affected by the coherent backscattering at larger phase angles.

444 Also, according to recent analytical and numerical models, the shadow hiding acts solely

445 on the linear part of the phase function (Stankevich et al., 1999; Shkuratov et al., 1999).
 446 We define here the absolute slope, whereas it is naturally a negative parameter, be-
 447 cause the phase function always decreases in brightness from 10° to 40° of phase angles
 448 (Kawata and Irvine, 1974; Stankevich et al., 1999; French et al., 2007).

449 The slope depends on the volume filling factor D and the optical depth of the slab
 450 (Kawata and Irvine, 1974; Stankevich et al., 1999). Two models has been developed for
 451 different regimes of the particle volume density D and predict opposite behavior of S
 452 as the function of D and τ .

453 The *shadowing* model of Irvine (1966) and Kawata and Irvine (1974), also called *inter-*
 454 *particle shadow hiding* by Goldreich and Tremaine (1978), consists in shadows of macro-
 455 scopic particles ($\bar{r}=15$ m, see Kawata and Irvine, 1974) in a particulate medium, such
 456 as $8D \ll 1$ (Irvine, 1966). The smaller the volume density D, the steeper the phase func-
 457 tion for increasing phase angle (Kawata and Irvine, 1974). Other refinements of this
 458 model exists (Esposito, 1979; Hapke, 1986; Stankevich et al., 1999; French et al., 2007)
 459 but lead to the same results : the opposition peak due to the shadowing sharpens and
 460 the absolute slope increases with decreasing packing density (or filling factor).

461 Another model exists, the *intra-particle shadow hiding*, which is valid for higher par-
 462 ticle volume density according to Goldreich and Tremaine (1978); Muinonen (1994).
 463 Buratti and Veverka (1985) underlined the fact that the mutual shadowing among re-
 464 golithic grains could be suited for understanding the textural properties of the regolith.
 465 As a consequence, this mechanism operates at the surface of ring material : e.g. in the
 466 regolith layer.

467 However, other physical parameters need to be taken into account. In the analytical
 468 *inter-particle shadow hiding* model of Hapke (2002), the slope can be linked to the an-
 469 gular width of the shadow hiding h_{sh} . Thus a normalized and absolute slope would
 470 be $S = \frac{1}{2h_{sh}} = \frac{D}{Q_{ext}(\lambda, \bar{r})\bar{r} \ln(1-D)}$, with D the volume filling factor, $Q_{ext}(\lambda, \bar{r})$ the ex-
 471 tinction coefficient and \bar{r} the mean radius of particles. Then, the slope should depend
 472 on the wavelength and on the particle size. Interestingly, laboratory experiments of

473 Kaasalainen (2003) showed that the slope increases when the sample's size increases.
474 However, the microscopic and/or macroscopic roughness of the medium need also to be
475 taken into account in the shadow hiding models, as underlined by Hapke (1984, 1986);
476 Shkuratov et al. (1999); Kaasalainen (2003) and Shepard and Helfenstein (2007). For
477 example, laboratory experiments of Kaasalainen (2003) showed that the slope increases
478 when the sample's roughness increases.
479 Then laboratory measurements and recent theoretical models could significantly in-
480 crease the number of physical parameters on which S depends.

481 From the above arguments, the HWHM and the amplitude A are governed by both co-
482 herent backscatter and shadow hiding effects whereas the slope S provides information of
483 the shadow hiding effect solely.

484 **3 Shape of the phase curves at opposition**

485 *3.1 The opposition effect in CLEAR filters*

486 Due to the automation of extraction and fitting procedures (cf section 2.2) and due to
487 the high images resolution, phase functions were extracted in as many as 211 different
488 locations, in the D, C, B rings, Cassini Division and A ring (in increasing distance from
489 Saturn, left column of Table 1 of Electronic supplementary material). In this section, we
490 first present the typical behavior of some selected phase curves in different regions of the
491 main rings (section 3.1.1), then we discuss similarities and differences and what are the
492 general trends from sections 3.1.2 to 3.1.4.

493 *3.1.1 Overview of the CLEAR phase curves*

494 Examples of phase curves in various ring regions are presented in Fig. 7. Each pair of
495 graphs show on the left side a zoom from 0.01 to 2.5 degrees and on the right side,
496 the fuller phase curve from 0 to 25 degrees. These curves were obtained by combining
497 several WAC images with a large distribution of viewing geometries (Table 1) each curve
498 is built from the merging of 10 to 70 different images with various values of emission angle,
499 incidence angle, phase angle etc. The dispersion of points is not due to the measurement
500 uncertainty but reflects mainly the limits of the Chandrasekhar (1960) inversion formula
501 that was used to extract the phase function from the measured values of I/F. It seems
502 that some important physics may be missing (like multiple scattering), that could explain
503 the scattering of points. Curves for the A and D rings (Fig. 7) are incomplete between 3
504 to 20° which is due to removal of images because of an artifact (cf section 2.1).

505 **[Fig. 7]**

506 Whereas the general shape is similar from one ring to another (Fig. 7), some details in the
507 shape may vary significantly. First pair of graphs in Fig. 7 shows the phase curve derived
508 in the D ring from images of *June 26*. Due to short exposure time (10 ms), the D ring
509 ringlets are too faint to be detected. In images of *June 26*, a bright spot is visible from
510 67 000 km to the inner boundary of the C ring : this corresponds to the expected location of
511 the background sheet of material constituting part of the D ring (Hedman et al., 2007a).
512 However camera artifact may be visible in such dim regions of the image but could not
513 be clearly identified here. So the fact that a strong increase of brightness at the expected
514 location of the opposition and the coherent variation of the signal with observing geometry
515 between different images suggest that we indeed see the opposition effect in the D ring.
516 However some doubts still remain. From 0.5 to 2 degrees, the curve is similar to other
517 rings. Below 0.5 degree an exponential surge and a flattening at zero degree distinguish
518 this phase function from the other ones. Does it reflect optical properties of D ring dust ?

519 Is it an artifact ? This plateau below 0.5 degree is much too large to be explained by
520 the finite angular radius of the Sun (0.025 degree). Because of these uncertainties, at this
521 point it is speculative to interpret this specific behavior as real.

522 For the C ring (Fig. 7), the shape of the phase function is well sampled below 2 degrees.
523 It is comparatively wider than in dense A and B rings. More precisely, HWHM of the
524 opposition surge is wider for the C ring (HWHM=0.26°) than for the A and B ring
525 (HWHM~0.20°). This could be also interpreted as a steeper slope of the linear regime of
526 the phase function for $\alpha > 2^\circ$. Wavy features between 5 to 25 degrees can be attributed
527 to images artifact. Their amplitude is about 15% of the total signal of the C ring.

528 The B ring opposition surge has the smallest amplitude of all rings ($A=1.25$ in Fig. 7). This
529 was already underlined by the recent study of French et al. (2007) whereas previous ob-
530 servations of Esposito et al. (1979) and Poulet et al. (2002) give the exact opposite trend.
531 However, their result could have a bias due to the lack of data below 0.3° of phase angle
532 for Poulet et al. (2002) and 0.1° for Esposito et al. (1979) whereas French et al. (2007)
533 had values much smaller (the smallest phase angles at which HST observed the B ring
534 range from 0.0037 to 0.0132 degrees French et al., 2007). The B ring has also the steepest
535 slope ($S=0.105 \varpi_0 P.\text{deg}^{-1}$) in the linear regime explaining why the opposition spot is so
536 contrasty in the ISS images.

537 The Cassini Division has a similar amplitude and width ($A\sim 1.47$ and HWHM~0.28° in
538 Fig. 7) to the C ring ($A\sim 1.45$ and HWHM~0.26° in Fig. 7). Their slope of the linear regime
539 are also similar ($S=0.033 \varpi_0 P.\text{deg}^{-1}$ for the Cassini Division and $S=0.030 \varpi_0 P.\text{deg}^{-1}$ for
540 the C ring). These similarities were first noticed by Poulet et al. (2002) and are suggestive
541 of a strong dependence of the opposition effect on the optical depth (we will come back
542 to this in section 3.1.4).

543 An example of the A ring phase function is given in the last pair of graphs in Fig. 7.
544 At first sight, the signal appears much more disturbed than in other rings : specifically,

545 pieces of phase functions extracted from different images show a wide dispersion in this
 546 graph, whereas signal from an individual image has a very low dispersion. The origin of
 547 this is not clear and may be due to the artifact reported in section 2. The dispersion
 548 of the data is about 15% of the signal whereas the camera artifact should represent at
 549 most 5% of the signal only (estimated on the background). It may be possible that the
 550 dispersion may be also due to an intrinsic photometric effect which is not corrected by
 551 the Chandrasekhar (1960) single scattering model (equation(1)). Indeed, the A ring has
 552 an intermediate optical depth ~ 0.5 so that it neither appears as a solid surface (like the
 553 B ring) or as a dilute system (like the C ring). Here, we are in an intermediate regime
 554 where many collective effects may influence strongly the apparent phase function (multiple
 555 scattering, gravitational wakes, density waves, etc.). A sophisticated model is required here
 556 to investigate such effect (Porco et al., 2007). However the general trends are quite clear
 557 and the A ring phase curve has a larger peak amplitude ($A=1.39$ in Fig. 7) than the B ring's
 558 ($A=1.25$ in Fig. 7). We see in addition that the slope of the linear regime is shallower in
 559 the A ring ($S=0.078 \varpi_0 P.\text{deg}^{-1}$ in Fig. 7) than in the B ring ($S=0.105 \varpi_0 P.\text{deg}^{-1}$ in
 560 Fig. 7) but steeper than in less dense rings ($S\sim 0.03 \varpi_0 P.\text{deg}^{-1}$ in Fig. 7). Thus the phase
 561 curve at opposition in the A ring is somewhat intermediate between the B and C rings,
 562 strengthening the idea of a dependence on the optical depth.

563 Finally, we conclude this section by remarking that the opposition effect is very diverse
 564 in Saturn's rings, and could be the consequence of different properties of the surface ring
 565 particles in various ring regions. Some general trends can be underlined, as we see in the
 566 next section.

567 In a first step, we check if some correlations exist between the morphological parameters
 568 which depend on the same portion of the curve (e.g. A and HWHM for the surge) and
 569 also if parameters describing different parts of the phase curve can be correlated (e.g. A ,
 570 HWHM and S for, respectively, the surge and the linear part). This is the purpose of the
 571 next section.

572 *3.1.2 Cross comparisons between morphological parameters*

573 In order to constrain the morphology of the surge, we correlate the amplitude A with the
574 angular width HWHM for the different main rings.

575 We fit A and HWHM with a linear function and found correlation coefficients reported in
576 Table 2.

577 **[Table 2]**

578 In Table 2 the Cassini Division, the amplitude A has the steepest function of the HWHM.
579 A linear fit gives a slope of about 1.2 with a correlation coefficient of 47 %. This mean
580 that narrow surges have a low amplitude and inversely wide surges have large amplitude.
581 In the C ring, values of A and HWHM are generally greater than in the Cassini Division
582 (but there are some exceptions). For the amplitude, this qualitative difference between the
583 Cassini Division and the C ring is confirmed by previous study of Poulet et al. (2002) and
584 French et al. (2007). For the angular width, although our trend of HWHM agrees with the
585 results of French et al. (2007), it contradicts previous work of Poulet et al. (2002), this is
586 certainly due to the overestimation of HWHM when the smallest phase angles are missing
587 (section 2.3.4 and Fig. 6b).

588 For the C ring, we find a slope for $A=f(\text{HWHM})$ of about 0.9 with a good correlation
589 coefficient of 79 %.

590 The A ring shows a similar variation of $A=f(\text{HWHM})$ as for the C ring (1.0) with a
591 correlation coefficient of 56 %.

592 Finally, A and HWHM in the B ring have values smaller than in the faint rings (C ring
593 and Cassini Division). Data points of A and HWHM for the B ring are concentrated
594 in a similar range as the A ring one, however with a much shallower slope (0.6 with a
595 correlation coefficient weakly reliable of 29 %, see Table 2). This means that the shape
596 of opposition phase curves in the B ring may have various angular width with an almost
597 constant value of the amplitude.

598 To conclude, the amplitude of the surge seems correlated with the angular width, at least
599 for the C ring, A ring and Cassini Division whereas the amplitude is independent of
600 HWHM for the B ring. The slope of $A=f(\text{HWHM})$ seems to decrease from the Cassini
601 Division to the B ring, passing by the C and A rings, suggesting that the slope is a
602 decreasing function of the optical depth.

603 Whereas the slope S on the one hand, A and HWHM on the other hand are thought
604 to be related to different portion of the phase curve (linear part and surge respectively),
605 it is interesting to note that they are somewhat correlated. We simply note that S is a
606 decreasing linear function the angular width and is also correlated with the amplitude.
607 Slopes and correlation coefficients of $S=f(A)$ and $S=f(\text{HWHM})$ are reported in Table 2.
608 This could be due to the fact that we derive our slope from 1.5° to 25° whereas analytical
609 model of Shkuratov et al. (1999), for example, describes the shadow hiding effect as a
610 slope which fits the phase curve from 4.5° to larger phase angles, see (Poulet et al., 2002).

611 3.1.3 Regional behavior

612 We now look for regional behavior inside each ring (Fig. 8). The Fig. 8 displays A , HWHM
613 and S as a function of the distance from Saturn by introducing a *ring type* nomenclature
614 based on the regional behavior of the C ring, well studied by Cooke (1991) and decomposed
615 into three *ring types* : inner ring, background and *plateaux*. We have modified and extended
616 this nomenclature to five classes of ring features, then applicable to the entire main rings
617 system :

- 618 (1) inner regions characterized by low optical depth in all the rings (for example, the dark
619 bands in the Cassini Division, see (Flynn and Cuzzi, 1989)),
- 620 (2) background are morphological smooth regions without abrupt variation of τ ,
- 621 (3) bright regions (*plateaux* or *plateaus* in the C ring (Holberg et al., 1982), density and
622 bending waves in the A ring located by Esposito et al. (1983)) are the regions in each

623 ring with the highest optical depth,
624 (4) *ringlets* according to Holberg et al. (1982) are thinner ring embedded in a less dense
625 region or a gap,
626 (5) outer regions (for example the so-called *ramp* for the C ring and the Cassini Division
627 (Cuzzi and Estrada, 1998)) mark the transition at the boundaries of each ring.

628 **[Fig. 8]**

629 In Fig. 8a and b, the amplitude A and the HWHM vary smoothly across the main ring
630 system (C to A rings), with only little scattering around the main trend (apart from
631 the Cassini Division), illustrating the stability of the linear-by-part model for comparing
632 multiple observations in different ring regions. From the C ring to the middle of the
633 B ring, a smooth decrease is observed. No sharp transition is observed between the C and
634 B rings. The outer regions of the C ring which are rich in gaps, plateaux and ringlets,
635 have a somewhat larger value of amplitude.

636 From the middle of the B ring to the outer of the A ring, both A and HWHM increase
637 again. The Cassini Division presents (1) larger values of A and HWHM as in the C ring
638 and (2) strongly dispersed values which may be indeed real because no image artifact is
639 visible in this Division.

640 The slope has a significantly different behavior (Fig. 8c) because strong jumps are observed
641 at the boundaries of each ring. This reinforces differences of behavior of the surge and the
642 linear part of the phase curve with the distance from Saturn.

643 As a result, the behavior of A, HWHM and S did not show significant variations with
644 ring type. Cooke (1991) noticed single scattering albedo of the C ring was dependent on
645 the ring type classification. Maybe that the absence of correlation between morphological
646 parameters and the ring type classification implies that the morphological parameters are
647 independent of the single scattering albedo. Since the single scattering albedo is correlated
648 with the optical depth, (Spilker et al., 2005), we try now to correlate the morphological

649 parameters with the optical depth in the next section.

650 3.1.4 *Optical depth variations of the morphological parameters*

651 In order to quantify differences in terms of morphological shape in our 211 phase curves
652 in CLEAR filters (see section 3.1.1), we use the three parameters A, HWHM and S. They
653 are represented in the Fig. 9 as a function of the normal optical depth of the rings.

654 **[Fig. 9]**

655 Because the overall correlations of A, and S HWHM with τ are not clear, although they
656 seem to lead to an negative correlation for A and HWHM (Fig. 9a,b) and a positive
657 correlation for S (Fig. 9c), we calculated with a linear fit the correlation coefficients for
658 $A=f(\tau)$, $HWHM=f(\tau)$ and $S=f(\tau)$ for each main ring, see Table 3.

659 **[Table 3]**

660 The amplitude A of the surge (Fig. 9a) is correlated with the optical depth of the rings. The
661 following trends may be noted : first, the amplitudes of low optical depth ($\tau < 0.5$, typically
662 the C ring and the Cassini Division) are positively correlated with the optical depth (Ta-
663 ble 3) and second, the amplitude at high optical depth ($\tau > 1$, typically the A and B rings)
664 are negatively correlated with the optical depth (Table 3). The second trend was quite clear
665 by eye, whereas the first one is more difficult to distinguish in Fig. 9a. This is due to the
666 fact that the C ring and the Cassini Division have an optical depth restricted in the range
667 $0.01 < \tau < 0.5$, which is quite compressed in the scale from 0 to 2.5 of Fig. 9. The same be-
668 havior (increasing of amplitude with increasing albedo, or τ , the two values are correlated
669 Doyle et al., 1989; Dones et al., 1993) was noticed by Belskaya and Shevchenko (2000) for
670 the amplitude of asteroids' phase curves : for albedo < 0.3 an increase of the amplitude with
671 increasing albedo was noticed.

672 We note also that for intermediate and high optical depth ($0.5 < \tau < 2.5$, typically the A

673 and B rings) the amplitude has a much smaller scattering and finally, the correlation co-
674 efficient are larger (-74% for the B ring).

675 For the A ring, it is interesting to note that regions of lower optical depth ($0.3 < \tau < 0.5$)
676 connect well with data-points in the C ring both in terms in mean value and scattering
677 (Fig. 9a). A good continuity with the B ring is also observed ($0.7 < \tau < 1.1$).

678 The angular half width of the peak at half maximum (Fig. 9b) show similar correlation
679 with the optical depth than the amplitude of the surge : increase of HWHM when the op-
680 tical depth increases for the C ring and the Cassini Division and decrease of HWHM
681 when the optical depth increases for the A and B rings. The scattering of HWHM
682 ($\text{HWHM} \sim 0.3 \pm 0.2$) for the low optical depth regions behaves similarly as for the ampli-
683 tude, and lead to small correlation coefficients (19%, see Table 3). As for the amplitude,
684 the scattering of HWHM is narrow for intermediate optical depth ($0.5 < \tau < 1.6$). Again, the
685 behavior of the A ring is clearly intermediate between the C and B rings. To summarize,
686 the behavior of HWHM is a decreasing function of increasing optical depth, with impor-
687 tant scattering at low τ that could be understood as an opposite behavior of HWHM
688 (HWHM is an increasing function of increasing optical depth).

689 The general trend for the slope of the linear regime (Fig. 9c) is a strong increase with in-
690 creasing optical depth, with a uniform scattering and with central value well represented
691 by $S \sim 0.07\tau^{1/2}$. This is the first time that a correlation is established between the slope S
692 and the optical depth. Previous morphological study on asteroids' solar phase curves
693 showed an exponential correlation between the slope of the phase function (the so-called
694 phase coefficient β in mag.deg^{-1}) and the albedo (Belskaya and Shevchenko, 2000). Our
695 trend for the slope (the increase of S in $\varpi_0 P.\text{deg}^{-1}$ with increasing τ) is thus consistent
696 with the slope of asteroids' phase functions (decrease of β in mag.deg^{-1} with increasing
697 albedo, recall that the magnitude M is inversely proportional to I/F , the so-called geo-
698 metric albedo : $I/F = 10^{-0.4M}$, see Domingue et al., 1995, so decrease of β in mag.deg^{-1}
699 with increasing albedo leads to increase of β in $I/F.\text{deg}^{-1}$ with increasing albedo), since we

700 assume that the optical depth is positively correlated with the albedo, as already noticed
701 by Doyle et al. (1989); Dones et al. (1993). However, as for A and HWHM, low optical
702 depth regions (as the C ring and the Cassini Division) have a distinct trend than the trend
703 of the A and B rings.

704 In conclusion, whereas the slope S has a strong tendency with the optical depth (the
705 average of the absolute correlation coefficients of $S=f(\tau)$, see values of Table 3) is 53%),
706 the first two parameters A and HWHM have a soft tendency with the optical depth (the
707 average of the absolute correlation coefficients for $A=f(\tau)$ is 44% and for $HWHM=f(\tau)$
708 is 32%). Consequently, Fig. 9 which presents A, HWHM and S according to the optical
709 depth, yields the following trends :

710 (1) The morphological parameters of the surge (A and HWHM) have both similar behavior
711 with τ in the C ring and the Cassini Division. Firstly, a positive correlation of A with
712 τ and of HWHM with τ , with a strong scattering and become almost independent
713 of the optical depth for $\tau > 0.5$. Secondly, we note a negative correlation of S with τ .
714 These trends are reversed (negative correlations of A and HWHM with τ and a positive
715 correlation of S with τ) for the moderate and high optical depth regions (typically the
716 A and B rings) ;

717 (2) the morphological parameter of the linear regime (S) is strongly positively correlated
718 with the optical depth : negatively correlated in the C ring and the Cassini Division
719 (where $\tau < 0.5$) and positively correlated in the A and B rings (where $\tau > 0.5$).

720 We conclude that the trends of all the morphological parameters are linked to the optical
721 depth. Then the drastic differences between, on the one hand, the amplitude and the
722 angular width of the surge and, on the other hand, the slope of the linear part across
723 the main ring system suggests that these characteristics originate from different physical
724 mechanisms, as predicted by physical models (see section 2.3.5).

725 3.2 *The opposition effect in COLOR filters*

726 3.2.1 *Overview of the COLOR phase curves*

727 Fig. 10 details examples of phase curves obtained for the C, B, A rings and the Cassini
728 Division. A striking result is that the COLOR phase curves' peaks are much narrower
729 than the CLEAR phase curves' peaks. Indeed, this is due to the fact that WAC images
730 (exclusively used for the CLEAR phase curves) do not have the more peaked part of the
731 phase function ($\alpha > 0.01^\circ$) whereas NAC images have it ($\alpha > 0.001^\circ$, see Fig. 4). To check
732 this, we plot in the first column (labeled a) of Fig. 10 the phase function obtained with
733 the camera WAC and in the second (labeled b) we plot the fuller phase function obtained
734 with all the NAC and WAC images combined. Indeed, Fig. 10 demonstrates that the value
735 of $\varpi_0 P(\alpha)$ when α tend towards 0° is greater in the panel (b) than in the panel (a).

736 **[Fig. 10]**

737 The fact that WAC images do not include the peakiest part of the opposition surge explains
738 also the difference between the peak's intensity of curves in Fig. 3 in CLEAR filters and
739 COLOR filters because when we processed images in CLEAR filters, there was no NAC
740 images. This explains also the shift in I/F at the minimum phase angle on NAC images
741 and WAC images of the same filter (Fig. 3). We observe that the shift in I/F between
742 NAC and WAC image is minimum in the blue filter (Fig. 3), which implies that the full
743 surge is contained in WAC images for this wavelength.

744 In general, we noticed that the general shape of the curve is similar to that obtained
745 previously : the C ring still has a fairly broad peak with a large amplitude (first pair of
746 graphs at the top of Fig. 10). The B ring exhibits also narrow peaks as those of CLEAR
747 filters comparatively to the other main rings (the second pair of graphs of Fig. 10). The
748 Cassini division (third pair of graphs of Fig. 10) shows again a lot of scattering, which
749 could be the consequence of the failure of the Chandrasekhar (1960) inversion when the

750 optical depth is not well known. Finally, the A ring, yet very dense, shows also scattering
751 for $\varpi_0 P(\alpha)$, which could be due to the gravitational wakes, see the last pair of graphs
752 in Fig. 10. Indeed, the Chandrasekhar (1960) inversion is very sensitive to the optical
753 depth, and the wakes are known to modify locally the value of τ (Colwell et al., 2006;
754 Hedman et al., 2007b).

755 *3.2.2 Results in COLOR filters and comparisons with the morphological behaviors of the* 756 *CLEAR filters*

757 We now consider the variation of morphological parameters $A(\lambda)$, $\text{HWHM}(\lambda)$ and $S(\lambda)$ in
758 CLEAR and COLOR filters with the distance from Saturn (see Fig. 11).

759 **[Fig. 11]**

760 The amplitude of the opposition in the outer parts of the C and A rings has a much broader
761 scattering in COLOR filters than in CLEAR filters (Fig. 11a). There is, unfortunately, not
762 enough radial coverage to generalize this effect across the C ring. The Cassini Division
763 also shows similar behavior for the dataset at high and low spectral resolution. In the
764 B ring, where there is a good radial coverage in COLOR filters, amplitudes of CLEAR
765 filters are much lower than the smallest amplitudes in COLOR (typically in the blue at
766 $\lambda=0.451 \mu\text{m}$), also noticed for the amplitudes in CLEAR and COLOR filters in the A
767 ring. This could be due to the exclusive use of the images of the WAC to resolve the
768 CLEAR opposition surge (section 3.2.1)

769 The half-width at half maximum of the peak shows a good agreement between the data in
770 CLEAR filters and COLOR filters (Fig. 11b). The values are the same order of magnitude
771 in all the rings and the regional effect is the same, except for the A ring where HWHM at
772 high spectral resolution (COLOR filters) decreases when the distance at Saturn increases
773 while at low spectral resolution (CLEAR filters), HWHM seems to start to grow.

774 Finally, for the slope S of the linear part of the phase function, we represent a normalized

775 slope in order to compare data from the CLEAR filters with data from the COLOR filters.
776 We follow the method of French et al. (2007) which divided the slope by the intensity of
777 the background, thus the normalized slope is S/B_1 for the linear-by-part model and now
778 has the deg^{-1} unit. In Fig. 11c we have for S similar behavior as a function from Saturn in
779 the inner A ring and the Cassini Division for data in CLEAR filters and in COLOR filters.
780 Finally, the B ring shows regional effects very different at high and low spectral resolution,
781 especially in the middle of the B ring, at 107 000 km (the most optically thick region)
782 where the CLEAR filters' slope is significantly overestimated compared to the slope in
783 the blue filter ($\lambda=0.451 \mu\text{m}$). In the same region, we also observed a strong scattering of
784 HWHM (Fig. 11b).

785 *3.2.3 Comparisons with multi-wavelength HST observations*

786 We now compare the Cassini data (Fig. 11) with Earth-based data. For this purpose, the
787 recent study of French et al. (2007) was chosen due to their small phase angles $\alpha > 0.028^\circ$
788 and one point below the minimum phase angle corresponding to the angular size of the
789 Sun. The phase curves of French et al. (2007) were obtained in I/F for the main rings
790 and adjusted with the linear-by-part model of Kaasalainen et al. (2001) which provided
791 morphological parameters A, HWHM and S for different wavelengths ranging from the
792 ultraviolet to infrared (see their figure 7).

793 We consider first the regional effects of morphological parameters derived by French et al. (2007)
794 with the WFPC2/HST instrument.

795 The dispersion observed by the HST for the three morphological parameters A, HWHM
796 and S in the C ring and the Cassini Division is also very clear with ISS (Fig. 11abc).
797 However, it should be noted for the C ring scattering observed with our data (especially
798 those in CLEAR filters) is highly localized (internal and external parts of the ring) and
799 not present in the central regions, corresponding to the background according to the ring
800 type classification of Cooke (1991).

801 In the B ring, French et al. (2007) noticed strong variations of A and S in the inner edge
802 which are absent for A and are present for S in the ISS data (Fig. 11a and c). For HWHM,
803 HST did not have the raise of HWHM in the middle of the ring that we observed (Fig. 11b).
804 For the slope, we observe in both data set a decrease of S from the inner edge to the middle
805 of the ring (Fig. 11c).

806 In the A ring, the regional trends for the amplitude A and the angular width HWHM are
807 similar for HST in ISS (Fig. 11a), but it is not the case for S. French et al. (2007) obtained
808 an almost constant value of S. The absolute value of the slope of French et al. (2007) in
809 all filters is roughly $S \sim 0.04 \text{ deg}^{-1}$. With ISS/Cassini (Fig. 11c), we observe two distinct
810 trends. First, S at high and low spectral resolution have similar values. Second, the regional
811 effect observed is the same : there is a decreasing trend with increasing distance from Sat-
812 urn. At the inner edge, $S \sim 0.025 \text{ deg}^{-1}$ and at the outer edge $S \sim 0.015 \text{ deg}^{-1}$. There is,
813 however, a different order of magnitude obtained by ISS/Cassini and WFPC2/HST which
814 could be due to lack of data at large phase angles for Earth-based observation. Indeed,
815 the factor 2 between the slope values is well explained by the overestimation of the slope
816 when the phase angle coverage stops at 6 degrees (section 2.3.4 and Fig. 6c).

817 Now, we turn on the comparison on the variations of the morphological parameters with
818 the wavelength, which leads to the following conclusions.

819 First, French et al. (2007) found weak variations of $A(\lambda)$ in the B ring. Indeed, figure 3
820 of French et al. (2007) shows weak wavelength-variations of the amplitude in the B ring,
821 and also in the A ring. Only one notable difference occurs in the ultraviolet. Overall,
822 French et al. (2007) observed a decrease of $A(\lambda)$ from the ultraviolet to the green, and
823 then an increase in the amplitude of the green to the infrared. This is not at all what
824 is observed for the amplitudes of ISS where a notable increase from blue to green and a
825 decrease in the infrared to the green (Fig. 11a). The values of $A(\lambda)$ for ISS/Cassini and
826 WFPC2/HST are anti-correlated.

827 For $\text{HWHM}(\lambda)$, French et al. (2007) remarked a strong decrease of the half-width at half

828 maximum when the wavelength increases, and in all the rings. No break in decreasing
829 $\text{HWHM}(\lambda)$ is observed by the HST. This decrease is very different of the behavior of
830 $\text{HWHM}(\lambda)$ with ISS/Cassini (Fig. 11b). Thus the variations of $\text{HWHM}(\lambda)$ presented here
831 are also unprecedented. There is firstly not a decrease but an increase of HWHM with
832 increasing wavelength. Second, the order of magnitude found is not the same. The angular
833 half-width obtained with WFPC2/HST are generally between 0.05° and 0.2° while those
834 of ISS are between 0.1° and 0.4° . This discrepancy could be the consequence of the relative
835 thickness of our phase functions due to the use of several images at similar phase angles
836 whereas French et al. (2007) did not have multiple recovered data because they obtained
837 one point per phase angle.

838 Finally, for $S(\lambda)$, the wavelength behavior of French et al. (2007) are consistent with those
839 of ISS/Cassini (S decreases from the blue to the red, and slightly increases in the infrared),
840 Fig. 11c. Strangely, this agreement shows a consistency of both data sets for variations
841 of the slope with a wavelength whereas the regional effects of S observed by the two
842 instruments are significantly different.

843 *3.2.4 Variations of the opposition effect with the wavelength and the optical depth*

844 We see that the morphological parameters depend on the optical depth (Fig. 9) and also
845 on the wavelength (Fig. 12).

846 **[Fig. 12]**

847 It is appropriate now to quantify the variations of $A(\lambda)$, $\text{HWHM}(\lambda)$ and $S(\lambda)$ by fitting
848 them with a linear model. We thus obtain for each COLOR phase curve of the rings two
849 linear functions (one from 0.451 to $0.568 \mu\text{m}$ and another from 0.568 to $0.752 \mu\text{m}$) which
850 fit the behavior of $A(\lambda)$ and two linear functions $\text{HWHM}(\lambda)$, with the same wavelength
851 boundaries. For the slope $S(\lambda)$, two linear functions are obtained (one from $0.451 \mu\text{m}$ to
852 $0.650 \mu\text{m}$ and from $0.650 \mu\text{m}$ to $0.752 \mu\text{m}$), see Fig. 13 for an example.

853 [Fig. 13]

854 For this study, is only kept the slope of each linear function (that we called the steepness),
855 that we correlated with the optical depth of the rings (the linear functions and their
856 correlation coefficients are given in Tables 4 and 5).

857 [Table 4, Table 5]

858 The slopes of $A(\lambda)$ and $HWHM(\lambda)$ show both an increase with the optical depth from the
859 blue to the green (Table 4).

860 From the green to the infrared, we note a decrease of $A(\lambda)$ with τ , but not for $HWHM(\lambda)$
861 which can increase or decrease with the optical depth.

862 However, the strongest trends are found for $S(\lambda)$ which lead to an decrease with τ of $S(\lambda)$
863 from the blue to the red and to an increase of $S(\lambda)$ from the red to the infrared. Values
864 are given in Table 5.

865 It is interesting to note the similar wavelength trends for A and $HWHM$, which are singu-
866 larly distinct of the wavelength trends of S . This confirms the fact that the morphological
867 parameters originate from different physical mechanisms, as predicted by the physical
868 models (section 2.3.5).

869 3.3 General trends of the opposition phase curves' morphology with the ISS data

870 To conclude the section 3, the ISS data set provides several trends of the opposition effect
871 in Saturn's rings which concern the :

- 872 (1) **regional behavior of A, HWHM and S across the main ring system** : indeed,
873 the classification of ring type features defined in section 3.1.3 shows that A and $HWHM$
874 vary continuously across the ring system (thus quite independently of the ring type
875 classification), whereas S varies abruptly at the boundaries of each ring (Fig. 8) ;
- 876 (2) **morphology of the rings' phase curves** : in section 3.1.4, strong dependences on

877 the optical depth of the rings of A, HWHM and S were established : anti-correlation of
878 A and HWHM with τ and correlation of S with τ (Fig. 9). A high scattering at low τ
879 and high τ is noticed for HWHM in CLEAR and COLOR phase curves ;

880 (3) **correlation between the morphological parameters** : we showed in the sec-
881 tion 3.1.2 that the parameters of the surge A and HWHM are correlated (Table 2),
882 whereas there is only a weak dependence of HWHM and S on the one hand, and A and
883 S on the other hand (Table 2) ;

884 (4) **variations of the morphological parameters in CLEAR and COLOR filters** :
885 we remarked in section 3.2.2 that the CLEAR amplitude is smaller than the COLOR
886 ones, because the CLEAR data set did not includes NAC images which generally capture
887 the highest part of the surge (Fig. 11). We showed also that the discrepancy in the slope
888 of French et al. (2007) is due to their phase angle coverages which did not cover the
889 larger phase angles. As a consequence, their slopes are overestimated, as predicted by
890 our study on the influence of incomplete data (section 2.3.4 and Fig. 6c) ;

891 (5) **variations of the morphological parameters with the wavelength and the**
892 **optical depth** : $A(\lambda)$ increases from the blue to the green (0.451 μm -0.568 μm) and
893 decreases from the green to the infrared (0.568 μm -752 μm), Fig. 12. This increase is
894 reinforced when the optical depth increases (Table 4) and is marked by a maximum value
895 of $A(\lambda)$ in the green regardless of the rings. $\text{HWHM}(\lambda)$ also increases from the blue to
896 the green, but no general trend is noticed from the green to the infrared (Table 4). $S(\lambda)$
897 decreases from the blue to the red (0.451 μm -650 μm), then rises from the red to the
898 near-infrared (0.650 μm -752 μm), Table 5. The wavelength-variation of S is then quite
899 distinct to that of the surge parameters (A and HWHM), then suggesting that they
900 may originate from different physical mechanisms.

901 4 Discussion

902 4.1 *A : a combination of the coherent backscattering with the shadow hiding ?*

903 We showed in section 3.1.4 that the amplitude of the surge had a specific behavior ac-
904 cording to the optical depth. With the model of Shkuratov et al. (1999), an estimation of
905 the amplitude is possible but refers only to the coherent backscattering enhancement.
906 Poulet et al. (2002) derived the following expression for the amplitude of the surge :
907 $A \sim 1 + e^{-d/L}/2$ where d is the effective radius of grains and L is the free mean path of
908 photons in the regolithic medium. It turns out that the amplitude could not be greater
909 than 1.5, which contradicts our morphological results (Fig. 11a). This variation might be
910 due to the shadow hiding effect which is not taken into account in this computation of
911 the amplitude.

912 4.2 *Variations of S with the optical depth*

913 In shadow hiding numerical simulations of Stankevich et al. (1999) that take into account
914 the optical depth and the filling factor, the absolute slope of the linear part has roughly
915 the same value when the optical depth is greater than 1, whatever the filling factor value.
916 This theoretical prediction is now confirmed by our results : we observed a saturation of
917 S at $\tau > 1$ (Fig. 9c).

918 Also, we observe with the ISS data (Fig. 11c) a wavelength-dependence of the slope S.
919 This behavior was predicted by the model of Hapke (2002) because S depends on the
920 extinction coefficient $Q_{\text{ext}}(\lambda, \bar{r})$ where \bar{r} is the mean radius of particles (see section 2.3.4).

921 4.3 *Linking photometric behaviors with dynamical concepts*

922 The present study, thanks to the quality of its data (radial and angular resolution), allows
923 us to highlight several observational facts never reported in the history of the observation
924 of the opposition effect in the Saturn's system. The slope, the angular width and the
925 amplitude of the rings' opposition phase curves are clearly correlated with the optical
926 depth of the rings (Fig. 9). Whereas a physical description of such a dependence would
927 need a full new physical model, we provide here some arguments explaining how the
928 optical depth may indeed influence these three parameters.

929 The optical depth is both a measure of the local volume filling factor of material, and
930 the local collisional activity. Indeed, basic analytical computation shows that the filling
931 factor of ring particle is proportional to τ/H (with τ standing for the optical depth and H
932 standing for the vertical height of the rings). So one may expect regions of higher optical
933 depth to have a much higher filling factor of particles. This is also in agreement with local
934 simulation of ring dynamics (Wisdom and Tremaine, 1988), that shows that the vertical
935 width of material increases with decrease optical depth, because of the lower efficiency of
936 collisional damping. So one may expect the filling factor of particles to be an increasing
937 function of the optical depth.

938 However, in the case the slope of the phase function for phase angles $>1^\circ$, analytical and
939 numerical models (Irvine, 1966; Kawata and Irvine, 1974; Stankevich et al., 1999) predict
940 that S should depend on the particle filling factor D and the vertical extension of the
941 layer of particles in such way that the steeper is the slope, the lower is the filling fac-
942 tor. Our morphological trends (Fig. 9c) seem unambiguously to contradict the theoretical
943 trends of these models because our highest slopes are found in the high optical depth
944 regions. Because high optical depth regions are known to have the highest filling factor
945 (Salo and Karjalainen, 2003), this implies that assumptions of diluted layers ($D \lesssim 0.3$ and
946 $8D \ll 1$ respectively for Stankevich et al., 1999; Kawata and Irvine, 1974) are not suited

947 to the Saturn’s rings.

948 As a consequence, the shadow hiding observed in the Saturn’s rings may result of *intra-*
949 *particle shadow hiding*, as stated by Buratti and Veverka (1985). Another possibility is
950 that the shadow hiding that operates in the rings are maintained in a “regime of trans-
951 parency” of particles (Lumme et al., 1987; Irvine et al., 1988) that dominates the shad-
952 owing effect due to packing density.

953 We now turn to the case of the HWHM and the amplitude. Whereas there is still a debate
954 on what determine their value (Mishchenko, 1992; Mishchenko and Dlugach, 1992a,b; Shkuratov et al., 199
955 Hapke, 2002), authors agree to link them the coherent-backscattering process, which may
956 be controlled by the regolith at the surface of ring particles (Poulet et al., 2002). Like for
957 planetary surfaces, the regolith is expected to be the result of space fractionation and
958 erosional processes at the surface of the ring-particles, due (in particular) to the on-going
959 collisional activity inside rings. Numerical studies of the dynamics of the ring-particles
960 have shown that the optical depth is a key parameter controlling the collisional activity
961 of rings. On the one hand, the number of collisions per orbit per particle is proportional
962 to τ (in the regime of low optical depth , see Wisdom and Tremaine, 1988), on the other
963 hand, the random velocity in a ring of thickness H is about $H \times \Omega$ (with Ω standing for the
964 local keplerian frequency). Since H is a decreasing function of τ , thus impact velocities
965 are lower in regions of high optical depth. In short, particles in low-optical depth regions
966 may suffer rare but violent collisions, conversely, in high-optical depth regions particles
967 suffer frequent but gentle collisions.

968 This may explain qualitatively why the HWHM and amplitude have different behavior in
969 the data (Fig. 8 and 9). However, impact velocities have a lower bound $\sim 2r \times \Omega$ (with r
970 standing for the particle’s radius) due to the keplerian shear across the diameter of a par-
971 ticle. This “shear dominated limit” is reached when the optical depth is high, typically for
972 $\tau > 1$. In such high filling factor regime the dynamics of collisions is entirely controlled by
973 the keplerian shear rather than by the random impact velocities. This may qualitatively

974 explain why values of HWHM and Amplitude seem constant for $\tau > 1$: in this regime, the
975 collisional activity being about independent of optical depth, the physical properties of
976 the regolith may be about constant which is indeed observed.

977 In conclusion, in the absence of self-consistent physical model of the opposition effect,
978 these qualitative arguments show that there are good reasons to believe that the optical
979 depth is a key factor determining the opposition effect in the ring through two different
980 mechanisms :

981 (1) the optical depth may influence the absolute slope S, assuming that shadow hiding is
982 the preponderant mechanism at phase angles $\alpha > 1^\circ$

983 (2) the optical depth may controls the HWHM and the amplitude (at phase angles $\alpha < 1^\circ$)
984 if the structure of the regolith is influenced by the collisional activity.

985 4.4 Comparison of the opposition effect in optical light and infrared light

986 A comparison of the solar phase curves of ISS/Cassini and the thermal phase curves of
987 CIRS/Cassini yields to the following trends :

988 (1) Altobelli et al. (2007) found a prominent opposition surge for the thermal phase curves
989 of the plateaux, well fitted by a logarithmic model. This is also the case of the solar
990 phase curves of the plateaux observed by ISS (Fig. 8a) ;

991 (2) Altobelli et al. (2007) found that the thermal phase curves of the *background* (regions
992 in the close environment of the plateaux) do not have opposition surge, whereas back-
993 ground has an opposition surge in the solar phase curves of ISS (Fig. 8a) ;

994 A priori, the emitted phase curves may not reflect the coherent backscatter effect (Altobelli et al., 2007)
995 because interferences of photons did not act on heat, and thus on infrared light. However,
996 a pure shadow hiding model such as (Lumme and Bowell, 1981) fails to reproduce the
997 CIRS opposition surge of the plateaux (in general the shadow hiding models did not

998 produce high surges, Stankevich et al., 1999). This could be the proof that the shadow
999 hiding cannot produce solely the opposition surge in emitted light and that the coherent
1000 backscatter could act on the shadow hiding mechanism, by multiplying the single scat-
1001 tered light component at small phase angles, as underlined by Hapke (2002).
1002 Interestingly, no similar surge were observed in the background (Altobelli et al., 2007),
1003 whereas both plateaus and background have an opposition surge in the solar phase curves
1004 of ISS. Because the background regions are more dim and reflective than the plateaus
1005 (background have smaller optical depth and higher albedo than plateaus which means
1006 they reflect more than they absorb, Cooke, 1991), this could explain why these regions
1007 did not have an opposition peak in emitted light.

1008 5 Conclusion

1009 We report here the main conclusions of this morphological study on the Saturn's rings
1010 opposition effect seen by ISS/Cassini :

1011(1) The amplitude A and the half angular width HWHM of the opposition surge decrease
1012 with increasing optical depth τ . A and HWHM may reflect both coherent backscat-
1013 tering and shadow hiding, because according to French et al. (2007) the morphological
1014 parameters of the surge are greater than their coherent backscatter counterparts ;

1015(2) All the morphological parameters are linked together. We find correlations between A
1016 and HWHM, between HWHM and S , and also between A and S , which imply that
1017 S could be more or less affected by the coherent backscattering. This could be due
1018 to the fact that we derive our slope from 1.5° to 25° whereas analytical model of
1019 Shkuratov et al. (1999) describes the shadow hiding effect as a slope which fits the
1020 phase curve from 4.5° to larger phase angles, see (Poulet et al., 2002).

1021(3) The absolute slope S of the linear part of the phase function increases with increasing
1022 optical depth τ (for optically thick rings) and shows distinct trends to the morpholog-

1023 ical surge parameters, which implies that this parameter is not totally affected by the
1024 coherent backscattering. As (Lumme et al., 1987; Irvine et al., 1988), we think that the
1025 Saturn’s rings could be in a regime of transparency of particles because the effect of
1026 packing density (decrease of S with increasing packing density) is not that expected for
1027 the Saturn’s rings (increase of S with optical depth, and if we assume that the optical
1028 depth and the packing density are correlated, increase of S with increasing packing
1029 density) ;

1030 (4) τ -dependence with the morphological parameters strengthen our assumptions saying
1031 that environmental effects are the key element determining the opposition effect because
1032 the optical depth is a direct measure of the collisional and dynamical activity in the
1033 surrounding of particles and is highly correlated with A, HWHM and S ;

1034 (5) Comparisons of ISS/Cassini solar phase curves and CIRS/Cassini thermal phase curves
1035 in the C ring show that the C ring’s plateaus can have a strong opposition surge both in
1036 solar and thermal phase curves whereas the C ring’s background has a strong opposition
1037 surge in the solar phase curve and no opposition surge in the thermal phase curve.

1038 (6) Wavelength variations of the amplitude A of the surge show a maximum in all the rings
1039 at $\lambda=0.568 \mu\text{m}$. The increase of A from 0.451 to 0.568 μm and the decrease of A from
1040 0.568 to 0.752 μm are reinforced with increasing τ ;

1041 (7) Wavelength variations of HWHM of the surge show also a maximum at $\lambda=0.568 \mu\text{m}$ but
1042 it is not systematic, HWHM can also increase from 0.568 μm to 0.752 μm . Moreover,
1043 there is no specific wavelength variations of HWHM with the optical depth ;

1044 (8) Wavelength variations of the slope S of the linear part imply that the shadow hiding
1045 depend on the wavelength, may be via the particle’s scattering cross-section of recent
1046 model (Hapke, 2002). The decrease of S from 0.451 to 0.650 μm and the increase of S
1047 from 0.650 to 0.752 μm are reinforced with increasing τ .

1048 The goal of this first paper was not to derive and quantify directly the physical properties
1049 obtained from the models. First, because there is a large set of models and it seemed more

1050 convenient to separate the morphological models to the more physical and sophisticated
1051 ones. Second, because recent physical models did not implement only the opposition ef-
1052 fect but the main photometric effects which occur in the full phase function, from 0 to
1053 180 degrees. Consequently, more investigations will be provided for this purpose by using
1054 full phase curves and photometric analytical models in the second paper. In the future, we
1055 hope to have the linear degree of polarization at the opposition to obtain more constrains
1056 on the ring particle' textures.

Acknowledgements

The authors would like to thank F. Poulet, C. Ferrari, S. Rodriguez and the two referees for useful comments that improved the quality of the paper. This work was supported by the French *Conseil R/egional de la Martinique*, the French *Centre National de Recherche Scientifique* (CNRS) and the Cassini Project.

References

- Altobelli, N., Spilker, L., Pilorz, S., Brooks, S., Edgington, S., Wallis, B., Flasar, M., Nov. 2007. C ring fine structures revealed in the thermal infrared. *Icarus* 191, 691–701.
- Belskaya, I. N., Shevchenko, V. G., Sep. 2000. Opposition Effect of Asteroids. *Icarus* 147, 94–105.
- Belskaya, I. N., Shevchenko, V. G., Kiselev, N. N., Krugly, Y. N., Shakhovskoy, N. M., Efimov, Y. S., Gaftonyuk, N. M., Cellino, A., Gil-Hutton, R., Dec. 2003. Opposition polarimetry and photometry of S- and E-type asteroids. *Icarus* 166, 276–284.
- Bobrov, M. S., 1970. Physical properties of Saturn’s rings. In: *Surfaces and interiors of planets and satellites*, edited by A. Dollfus (Academic, New York). pp. 376–461.
- Buratti, B. J., Veverka, J., Nov. 1985. Photometry of rough planetary surfaces - The role of multiple scattering. *Icarus* 64, 320–328.
- Chandrasekhar, S., 1960. *Radiative transfer*. New York: Dover, 1960.
- Colwell, J. E., Esposito, L. W., Sremčević, M., Apr. 2006. Self-gravity wakes in Saturn’s A ring measured by stellar occultations from Cassini. *Geophysics Research Letters* 33, 7201–+.
- Cooke, M. L., 1991. Saturn’s rings: Photometric studies of the C Ring and radial variation in the Keeler Gap. Ph.D. thesis, AA(Cornell Univ., Ithaca, NY.).
- Cuzzi, J. N., Estrada, P. R., Mar. 1998. Compositional Evolution of Saturn’s Rings Due to Meteoroid Bombardment. *Icarus* 132, 1–35.
- Cuzzi, J. N., French, R. G., Dones, L., Jul. 2002. HST Multicolor (255-1042 nm) Photometry of Saturn’s Main RingsI: Radial Profiles, Phase and Opening Angle Variations, and Regional Spectra. *Icarus* 158, 199–223.
- Déau, E., Dones, L., Charnoz, S., Brahic, A., Mar. 2008. Is the Opposition Surge Morphology a Relevant Diagnosis of the Knowledge of Atmosphereless Planetary Surface? In: *Lunar and Planetary Institute Conference Abstracts*. Vol. 39 of Lunar and Planetary Inst. Technical Report. pp. 1498–+.

- Domingue, D. L., Lockwood, G. W., Thompson, D. T., Jun. 1995. Surface textural properties of icy satellites: A comparison between Europa and Rhea. *Icarus* 115, 228–249.
- Dones, L., Cuzzi, J. N., Showalter, M. R., Sep. 1993. Voyager Photometry of Saturn's A Ring. *Icarus* 105, 184–215.
- Doyle, L. R., Dones, L., Cuzzi, J. N., Jul. 1989. Radiative transfer modeling of Saturn's outer B ring. *Icarus* 80, 104–135.
- Esposito, L. W., Jul. 1979. Extensions to the classical calculation of the effect of mutual shadowing in diffuse reflection. *Icarus* 39, 69–80.
- Esposito, L. W., Harris, C. C., Simmons, K. E., Mar. 1987. Features in Saturn's rings. *Astrophysical Journal Supplement Series* 63, 749–770.
- Esposito, L. W., Lumme, K., Benton, W. D., Martin, L. J., Ferguson, H. M., Thompson, D. T., Jones, S. E., Sep. 1979. International planetary patrol observations of Saturn's rings. II - Four color phase curves and their analysis. *Astronomical Journal* 84, 1408–1415.
- Esposito, L. W., Ocallaghan, M., West, R. A., Dec. 1983. The structure of Saturn's rings - Implications from the Voyager stellar occultation. *Icarus* 56, 439–452.
- Ferrari, C., 1992. Variations azimutales de brillance des anneaux planétaires. Ph.D. thesis, FR(Université Paris XI, Orsay).
- Flynn, B. C., Cuzzi, J. N., Nov. 1989. Regular structure in the inner Cassini Division of Saturn's rings. *Icarus* 82, 180–199.
- French, R. G., Verbiscer, A., Salo, H., McGhee, C., Dones, L., Jun. 2007. Saturn's Rings at True Opposition. *The Publications of the Astronomical Society of the Pacific* 119, 623–642.
- Goldreich, P., Tremaine, S., May 1978. The velocity dispersion in Saturn's rings. *Icarus* 34, 227–239.
- Hapke, B., Jul. 1984. Bidirectional reflectance spectroscopy. III - Correction for macroscopic roughness. *Icarus* 59, 41–59.
- Hapke, B., Aug. 1986. Bidirectional reflectance spectroscopy. IV - The extinction coeffi-

- cient and the opposition effect. *Icarus* 67, 264–280.
- Hapke, B., Jun. 2002. Bidirectional Reflectance Spectroscopy⁵. The Coherent Backscatter Opposition Effect and Anisotropic Scattering. *Icarus* 157, 523–534.
- Hapke, B., Nelson, R., Smythe, W., May 1998. The Opposition Effect of the Moon: Coherent Backscatter and Shadow Hiding. *Icarus* 133, 89–97.
- Hedman, M. M., Burns, J. A., Showalter, M. R., Porco, C. C., Nicholson, P. D., Bosh, A. S., Tiscareno, M. S., Brown, R. H., Buratti, B. J., Baines, K. H., Clark, R., May 2007a. Saturn’s dynamic D ring. *Icarus* 188, 89–107.
- Hedman, M. M., Nicholson, P. D., Salo, H., Wallis, B. D., Buratti, B. J., Baines, K. H., Brown, R. H., Clark, R. N., Jun. 2007b. Self-Gravity Wake Structures in Saturn’s A Ring Revealed by Cassini VIMS. *Astronomical Journal* 133, 2624–2629.
- Helfenstein, P., Veverka, J., Hillier, J., Jul. 1997. The Lunar Opposition Effect: A Test of Alternative Models. *Icarus* 128, 2–14.
- Holberg, J. B., Forrester, W. T., Lissauer, J. J., May 1982. Identification of resonance features within the rings of Saturn. *Nature* 297, 115–120.
- Irvine, W. M., 1966. The shadowing effect in diffuse reflection. *Journal of Geophysical Research* 71, 2931–2937.
- Irvine, W. M., Muinonen, K., Lumme, K., Jun. 1988. Is the Mutual Shadowing Explanation for the Opposition Effect of Saturn’s Rings Still Valid? In: *Bulletin of the American Astronomical Society*. Vol. 20 of *Bulletin of the American Astronomical Society*. pp. 853–+.
- Kaasalainen, S., Oct. 2003. Laboratory photometry of planetary regolith analogs. I. Effects of grain and packing properties on opposition effect. *Astronomy and Astrophysics* 409, 765–769.
- Kaasalainen, S., Muinonen, K., Piironen, J., Aug. 2001. Comparative study on opposition effect of icy solar system objects. *Journal of Quantitative Spectroscopy and Radiative Transfer* 70, 529–543.
- Kawata, Y., Irvine, W. M., 1974. Models of Saturn’s rings which satisfy the optical ob-

- servations. In: Woszczyk, A., Iwaniszewska, C. (Eds.), *Exploration of the Planetary System*. Vol. 65 of IAU Symposium. pp. 441–464.
- Lumme, K., Bowell, E., Nov. 1981. Radiative transfer in the surfaces of atmosphereless bodies. I - Theory. *Astronomical Journal* 86, 1694–1721.
- Lumme, K., Irvine, W. M., Oct. 1976. Photometry of Saturn’s rings. *Astronomical Journal* 81, 865–893.
- Lumme, K., Muinonen, K., Peltoniemi, J., Karttunen, H., Bowell, E., Jun. 1987. A Possible Explanation for Anomalously Sharp Opposition Effects. In: *Bulletin of the American Astronomical Society*. Vol. 19 of *Bulletin of the American Astronomical Society*. pp. 850–+.
- Lumme, K., Peltoniemi, J., Irvine, W. M., 1990. Some photometric techniques for atmosphereless solar system bodies. *Advances in Space Research* 10, 187–193.
- Mishchenko, M. I., Aug. 1992. The angular width of the coherent back-scatter opposition effect - an application to icy outer planet satellites. *Astrophysics and Space Science* 194, 327–333.
- Mishchenko, M. I., Dlugach, Z. M., Jan. 1992a. Can weak localization of photons explain the opposition effect of Saturn’s rings? *Monthly Notices of the Royal Astronomical Society* 254, 15P–18P.
- Mishchenko, M. I., Dlugach, Z. M., Mar. 1992b. The amplitude of the opposition effect due to weak localization of photons in discrete disordered media. *Astrophysics and Space Science* 189, 151–154.
- Mishchenko, M. I., Rosenbush, V. K., N., K. N., 2006. Weak localization of electromagnetic waves and opposition phenomena exhibited by high-albedo atmosphereless solar system objects. *Applied Optics* 45, 4459–4463.
- Muinonen, K., 1994. Coherent Backscattering by Solar System Dust Particles. In: Milani, A., di Martino, M., Cellino, A. (Eds.), *Asteroids, Comets, Meteors 1993*. Vol. 160 of IAU Symposium. pp. 271–+.
- Muinonen, K., Zubko, E., Tyynelä, J., Shkuratov, Y. G., Videen, G., Jul. 2007. Light

- scattering by Gaussian random particles with discrete-dipole approximation. *Journal of Quantitative Spectroscopy and Radiative Transfer* 106, 360–377.
- Müller, G., 1885. Resultate aus Helligkeitsmessungen des Planeten Saturn. *Astronomische Nachrichten* 110, 225–+.
- Müller, G., 1893. Helligkeitsbestimmungen der grossen Planeten und einiger Asteroiden. *Publikationen des Astrophysikalischen Observatoriums zu Potsdam* 30, 198–389.
- Murray, C. D., Dermott, S. F., Feb. 2000. *Solar System Dynamics*. *Solar System Dynamics*, ISBN 0521575974, UK: Cambridge University Press, 2000.
- Nelson, R. M., Hapke, B. W., Brown, R. H., Spilker, L. J., Smythe, W. D., Kamp, L., Borzta, M. C., Leader, F., Matson, D. L., Edgington, S., Nicholson, P. D., Filacchione, G., Clark, R. N., Bibring, J.-P., Baines, K. H., Buratti, B. J., Bellucci, G., Capaccioni, F., Cerroni, P., Combes, M., Coradini, A., Cruikshank, D. P., Drossart, P., Formisano, V., Jaumann, R., Langevin, Y., McCord, T. B., Mennella, V., Sicardy, B., Sotin, C., Mar. 2006. Cassini Observations of the Opposition Effect of Saturn’s Rings-1. In: Mackwell, S., Stansbery, E. (Eds.), *37th Annual Lunar and Planetary Science Conference*. Vol. 37 of *Lunar and Planetary Inst. Technical Report*. pp. 1461–+.
- Nelson, R. M., Hapke, B. W., Smythe, W. D., Spilker, L. J., Oct. 2000. The Opposition Effect in Simulated Planetary Regoliths. Reflectance and Circular Polarization Ratio Change at Small Phase Angle. *Icarus* 147, 545–558.
- Nicholson, P. D., Cooke, M. L., Pelton, E., Oct. 1990. An absolute radius scale for Saturn’s rings. *Astronomical Journal* 100, 1339–1362.
- Petrova, E. V., Tishkovets, V. P., Jockers, K., May 2007. Modeling of opposition effects with ensembles of clusters: Interplay of various scattering mechanisms. *Icarus* 188, 233–245.
- Pollack, J. B., Oct. 1975. The rings of Saturn. *Space Science Reviews* 18, 3–93.
- Porco, C. C., Pantazopoulou, M. J., Richardson, D., Quinn, T., Kehoe, T. J. J., Sep. 1999. Light Scattering in Planetary Rings: the Nature of Saturn’s Particle Disk. In: *AAS/Division for Planetary Sciences Meeting Abstracts*. Vol. 31 of *AAS/Division for*

- Planetary Sciences Meeting Abstracts. p. 44.03.
- Porco, C. C., Weiss, J., Richardson, D. C., Dones, L., Quinn, T., Throop, H., 2007. Light Scattering in Saturn's Rings I: Basic Formulation, Ring Thickness, and the A Ring Azimuthal Asymmetry. Submitted to *Astron. J.*
- Porco, C. C., West, R. A., Squyres, S., McEwen, A., Thomas, P., Murray, C. D., Delgenio, A., Ingersoll, A. P., Johnson, T. V., Neukum, G., Veverka, J., Dones, L., Brahic, A., Burns, J. A., Haemmerle, V., Knowles, B., Dawson, D., Roatsch, T., Beurle, K., Owen, W., Dec. 2004. Cassini Imaging Science: Instrument Characteristics And Anticipated Scientific Investigations At Saturn. *Space Science Reviews* 115, 363–497.
- Poulet, F., Cuzzi, J. N., French, R. G., Dones, L., Jul. 2002. A Study of Saturn's Ring Phase Curves from HST Observations. *Icarus* 158, 224–248.
- Rabinowitz, D. L., Schaefer, B. E., Tourtellotte, S. W., 2007. The Diverse Solar Phase Curves of Distant Icy Bodies. I. Photometric Observations of 18 Trans-Neptunian Objects, 7 Centaurs, and Nereid. *Astronomical Journal* 133, 26–43.
- Richardson, D. C., Jul. 1994. Tree Code Simulations of Planetary Rings. *Monthly Notices of the Royal Astronomical Society* 269, 493–+.
- Rosenbush, V., Kiselev, N., Avramchuk, V., 2006. Similarity and diversity in photometric and polarimetric opposition effects of small Solar System bodies. *Journal of Quantitative Spectroscopy and Radiative Transfer* 100, 325–339.
- Salo, H., Oct. 1992. Gravitational wakes in Saturn's rings. *Nature* 359, 619–621.
- Salo, H., Oct. 1995. Simulations of dense planetary rings. III. Self-gravitating identical particles. *Icarus* 117, 287–312.
- Salo, H., Karjalainen, R., Aug. 2003. Photometric modeling of Saturn's rings I. Monte Carlo method and the effect of nonzero volume filling factor. *Icarus* 164, 428–460.
- Seeliger, H., 1884. Zur Photometrie des Saturnringses. *Astronomische Nachrichten* 109, 305–+.
- Seeliger, H., 1887. Zur Theorie der Beleuchtung der grossen Planeten insbesondere des Saturn. *Abhandl. Bayer. Akad. Wiss. Math.-Naturvw.* KLII 16, 405–516.

- Shepard, M. K., Helfenstein, P., Mar. 2007. A test of the Hapke photometric model. *Journal of Geophysical Research (Planets)* 112 (11), 3001–+.
- Shkuratov, I. G., Feb. 1991. The effect of the finiteness of the angular dimensions of a light source on the magnitude of the opposition effect of the luminosity of atmosphereless bodies. *Astronomicheskii Vestnik* 25, 71–75.
- Shkuratov, Y., Bondarenko, S., Kaydash, V., Videen, G., Muñoz, O., Volten, H., Jul. 2007. Photometry and polarimetry of particulate surfaces and aerosol particles over a wide range of phase angles. *Journal of Quantitative Spectroscopy and Radiative Transfer* 106, 487–508.
- Shkuratov, Y. G., Kreslavsky, M. A., Ovcharenko, A. A., Stankevich, D. G., Zubko, E. S., Pieters, C., Arnold, G., Sep. 1999. Opposition Effect from Clementine Data and Mechanisms of Backscatter. *Icarus* 141, 132–155.
- Showalter, M. R., Pollack, J. B., Ockert, M. E., Doyle, L. R., Dalton, J. B., Dec. 1992. A photometric study of Saturn’s F Ring. *Icarus* 100, 394–411.
- Simonelli, D. P., Buratti, B. J., Nov. 2004. Europa’s opposition surge in the near-infrared: interpreting disk-integrated observations by Cassini VIMS. *Icarus* 172, 149–162.
- Spilker, L. J., Pilorz, S. H., Edgington, S. G., Wallis, B. D., Brooks, S. M., Pearl, J. C., Flasar, F. M., Jun. 2005. Cassini CIRS Observations of a Roll-Off in Saturn Ring Spectra at Submillimeter Wavelengths. *Earth Moon and Planets* 96, 149–163.
- Stankevich, D. G., Shkuratov, Y. G., Muinonen, K., 1999. Shadow hiding effect in inhomogeneous layered particulate media. *J. Quant. Spectrosc. Radiat. Transfer* 63, 445–448.
- Verbiscer, A., French, R., Showalter, M., Helfenstein, P., Feb. 2007. Enceladus: Cosmic Graffiti Artist Caught in the Act. *Science* 315, 815–.
- Verbiscer, A. J., French, R. G., McGhee, C. A., Jan. 2005. The opposition surge of Enceladus: HST observations 338-1022 nm. *Icarus* 173, 66–83.
- Wisdom, J., Tremaine, S., Mar. 1988. Local simulations of planetary rings. *Astronomical Journal* 95, 925–940.

Table 1

Main observational parameters of each sequence of images for each geometry of observation ($i = \arccos(\mu)$ and $\epsilon = \arccos(\mu_0)$). CLEAR (WAC) filters designate the broadband filters in the optical domain (the central wavelength is $\lambda_{\text{cl}}^{\text{WAC}} = 0.611\mu\text{m}$). COLOR (NAC) filters designate blue, green, red and near infrared filters (at central wavelengths of $\lambda_{\text{bl}}^{\text{NAC}} = 0.440\mu\text{m}$ and $\lambda_{\text{bl}}^{\text{NAC}} = 0.451\mu\text{m}$; $\lambda_{\text{grn}}^{\text{NAC}} = 0.568\mu\text{m}$; $\lambda_{\text{red}}^{\text{NAC}} = 0.650\mu\text{m}$; $\lambda_{\text{ir}}^{\text{NAC}} = 0.752\mu\text{m}$) and COLOR (WAC) filters designate blue, green, red and near infrared filters (at central wavelengths of $\lambda_{\text{bl}}^{\text{WAC}} = 0.460\mu\text{m}$; $\lambda_{\text{grn}}^{\text{WAC}} = 0.567\mu\text{m}$; $\lambda_{\text{red}}^{\text{WAC}} = 0.649\mu\text{m}$; $\lambda_{\text{ir}}^{\text{WAC}} = 0.742\mu\text{m}$).

date	Nb im	i ($^{\circ}$)	ϵ ($^{\circ}$)	Radial res. (km.pix $^{-1}$)	Azim. res. (km.pix $^{-1}$)	Filters (Camera)
<i>June 7</i> 2005	12	111.5	111.9	44.0	115.1	CLEAR (WAC)
<i>June 26</i> 2005	66	111.3	111.3	30.1	70.0	CLEAR (WAC)
<i>July 23</i> 2006	48	73.1	73.4	13.4	40.7	CLEAR (WAC)
<i>May 20</i> 2005	57	111.6	111.6	4.6	11.5	COLOR (NAC)
<i>May 20</i> 2005	59	111.5	111.9	44.0	115.1	COLOR (WAC)
<i>Dec 31</i> 2006	12	104.4	108.7	38.4	104.8	COLOR (WAC)
<i>Feb 20</i> 2007	20	103.7	122.7	66.3	72.5	COLOR (WAC)
<i>Apr 25</i> 2007	16	102.7	110.7	44.4	92.6	COLOR (WAC)

Table 2

Results of linear fits (function and correlation coefficient) obtained for $A=f(\text{HWHM})$, $S=f(A)$ and $S=f(\text{HWHM})$ for each Saturn's main ring and using CLEAR phase curves.

	A=f(HWHM)		S=f(A)		S=f(HWHM)	
	function	correl.	function	correl.	function	correl.
Cass. Div.	$0.91 + 1.72\tau$	59 %	$0.04 - 0.03\tau$	-68 %	$0.049 - 0.05\tau$	-35 %
C ring	$1.20 + 0.91\tau$	79 %	$0.04 - 0.06\tau$	-46 %	$0.025 - 0.04\tau$	-47 %
A ring	$1.12 + 1.08\tau$	56 %	$0.10 - 0.14\tau$	-84 %	$0.079 - 0.24\tau$	-81 %
B ring	$1.18 + 0.58\tau$	31 %	$0.15 - 0.33\tau$	-79 %	$0.141 - 0.81\tau$	-65 %

Table 3

Results of linear fits obtained (function and correlation coefficient) for $A=f(\tau)$, $HWHM=f(\tau)$ and $S=f(\tau)$ for each Saturn's main ring and using CLEAR phase curves.

	$A=f(\tau)$		$HWHM=f(\tau)$		$S=f(\tau)$	
	function	correl.	function	correl.	function	correl.
Cass. Div.	$1.22 + 0.937$	41 %	$0.20 + 0.175\tau$	19 %	$0.040 - 0.030\tau$	-42 %
C ring	$1.50 + 0.024$	25 %	$0.33 + 0.077\tau$	19 %	$0.024 - 0.026\tau$	-68 %
A ring	$1.50 - 0.175$	-36 %	$0.31 - 0.106\tau$	-49 %	$0.024 + 0.025\tau$	19 %
B ring	$1.42 - 0.068$	-74 %	$0.24 - 0.016\tau$	-39 %	$0.035 + 0.031\tau$	82 %

Table 4

Results of linear fits (function and correlation coefficient) obtained for the steepness of $A(\lambda)=f(\tau)$ and for the steepness of $\text{HWHM}(\lambda)=f(\tau)$ using COLOR phase curves of the A and B rings ($\tau>0.5$).

	Steepness of $A(\lambda)=f(\tau)$		Steepness of $\text{HWHM}(\lambda)=f(\tau)$	
	function	correl.	function	correl.
$0.451 \mu\text{m} < \lambda < 0.568 \mu\text{m}$	$1.210 + 0.3\tau$	55 %	$0.14 + 0.011\tau$	38 %
$0.568 \mu\text{m} < \lambda < 0.752 \mu\text{m}$	$0.001 - 0.5\tau$	-51 %	$0.04 - 0.037\tau$	-46 %

Table 5

Results of linear fits (function and correlation coefficient) obtained for the steepness of $S(\lambda)=f(\tau)$ and the steepness of $S/B_1(\lambda)=f(\tau)$ using COLOR phase curves of the A and B rings ($\tau>0.5$).

	Steepness of $S(\lambda)=f(\tau)$ (in $\varpi_0 P.\text{deg}^{-1}.\mu\text{m}^{-1}$)		Steepness of $S/B_1(\lambda)=f(\tau)$ (in $\text{deg}^{-1}.\mu\text{m}^{-1}$)	
	function	correl.	function	correl.
$0.451 \mu\text{m} < \lambda < 0.650 \mu\text{m}$	$-0.21 - 0.043\tau$	-73 %	$-0.04 - 0.039\tau$	-49 %
$0.650 \mu\text{m} < \lambda < 0.752 \mu\text{m}$	$0.04 + 0.018\tau$	67 %	$0.02 + 0.054\tau$	44 %

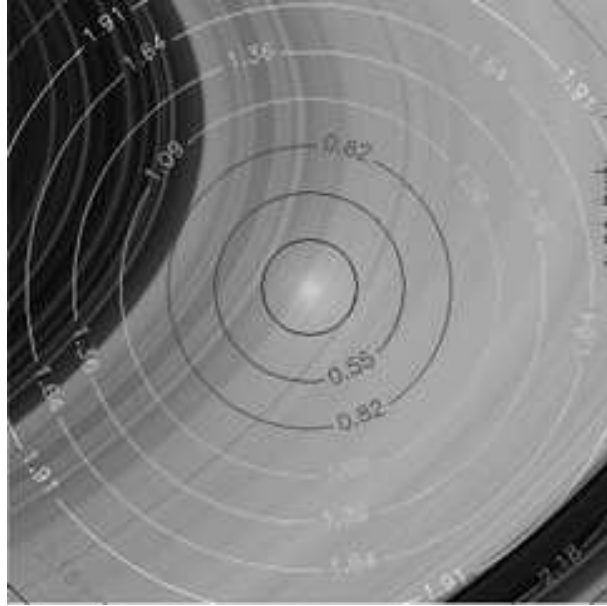


Fig. 1. The opposition effect in the B ring. A typical image of the *26 June* sequence captured by the Wide Angle Camera (W1498453136.IMG). Concentric circles correspond to identical phase curves computed in the image (isophase). Numbers in the concentric circles represent the solar phase angles (in degrees).

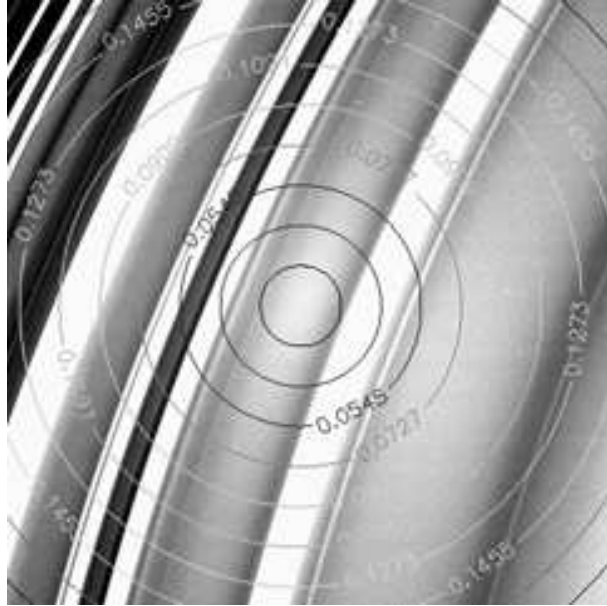


Fig. 2. The opposition effect in the C ring. A typical image of the *20 may* sequence captured by the Narrow Angle Camera (N1595278165.IMG). The contrast is enhanced to make more visible the opposition spot in the C ring. Concentric circles correspond to identical phase curves computed in the image (isophase). Numbers in the concentric circles represent the solar phase angles (in degrees).

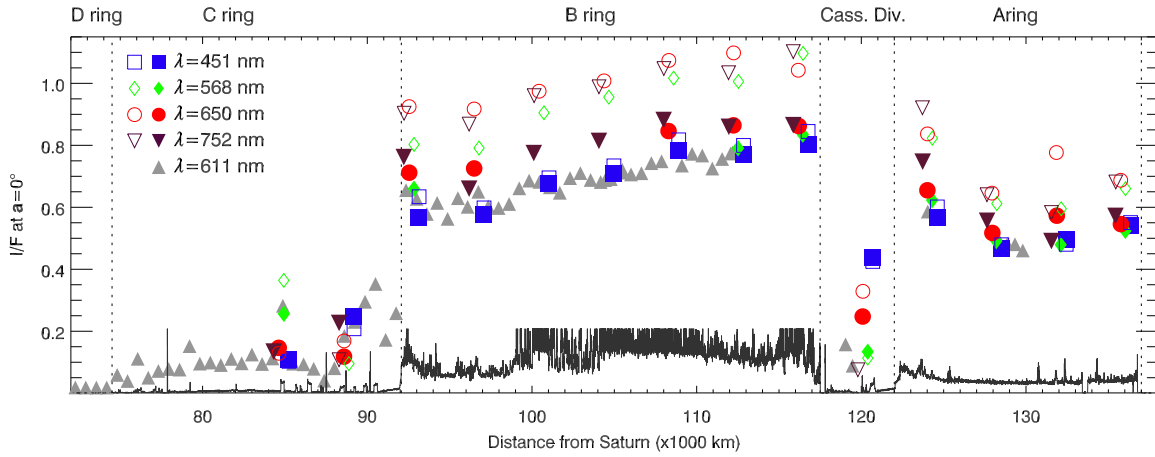


Fig. 3. Radial location of the opposition spot in the images taken in CLEAR and COLOR filters (filled symbols represent WAC images and empty symbols represent NAC images). We give in the y -axis the normalized brightness I/F of the minimum phase angle in the image, the x -axis is the corresponding distance from Saturn of this point. The vertical dotted lines correspond to ring boundaries. The optical depth of PPS/Voyager is plotted as a radial reference.

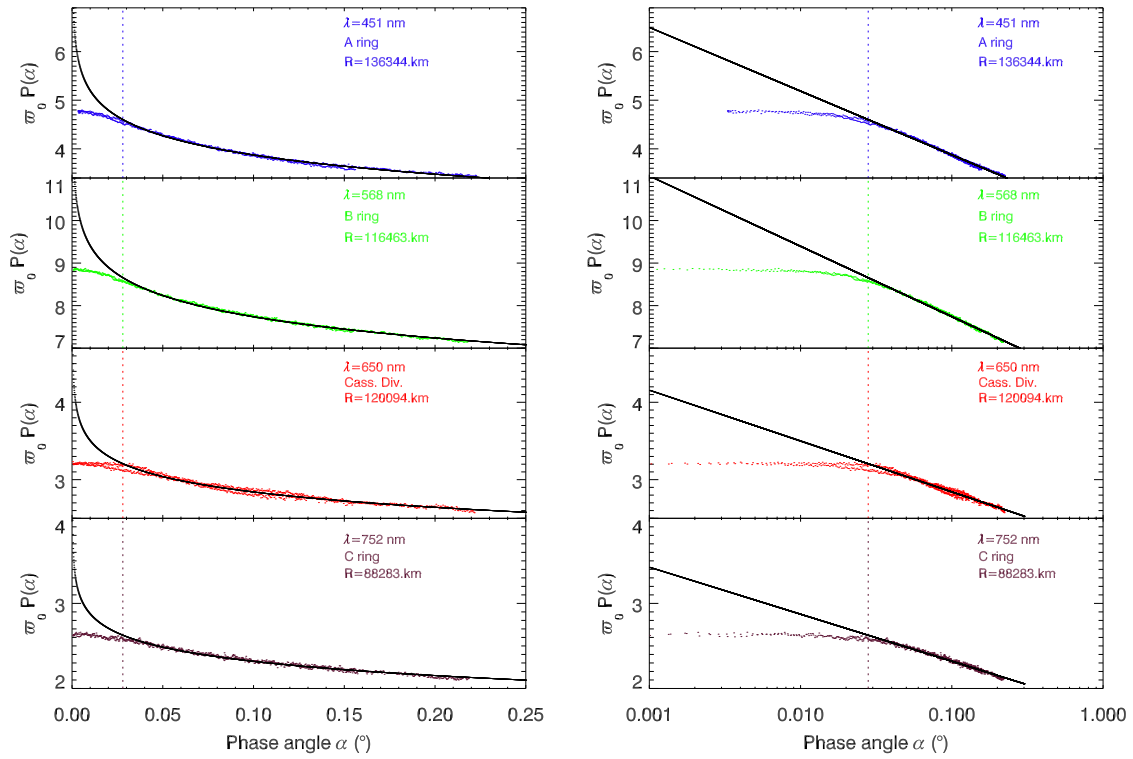


Fig. 4. Extracted COLOR phase curve from NAC images of the *May 20* sequence in A, B, C rings and Cassini Division in linear scale (a) and logarithmic scale (b). The vertical dotted line in (a) and (b) corresponds to the angular size of the Sun. The solid curves in (a) and (b) correspond to the logarithmic model of Bobrov (1970).

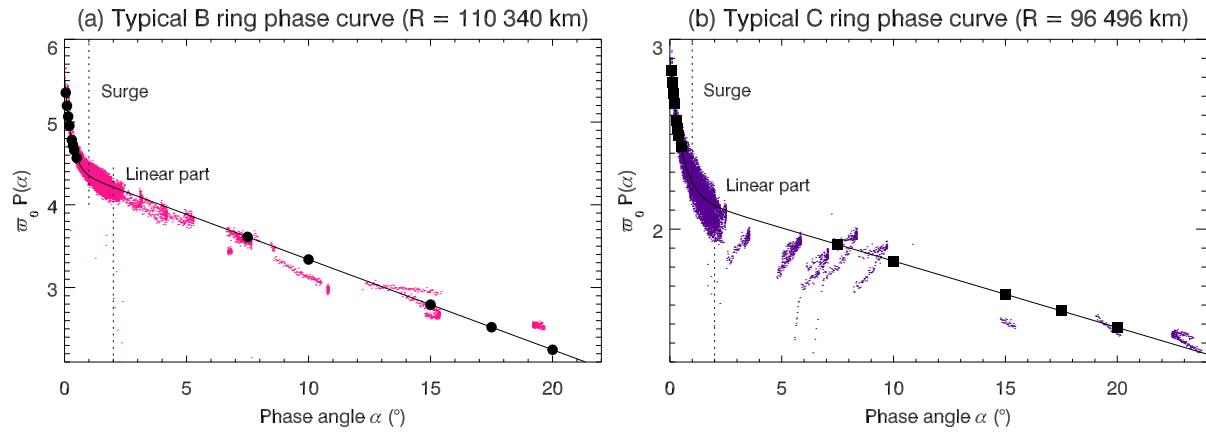


Fig. 5. Typical phase curves of the B ring (a) and C ring (b) in CLEAR filters chosen for testing the stability of linear-exponential model of Kaasalainen et al. (2001) when the phase angle coverage is incomplete. Circles and squares correspond to the cutoff of the incomplete phase function and the solid curves correspond to the initial fit of the linear-exponential model of Kaasalainen et al. (2001). The vertical dotted lines correspond to boundaries of the surge domain and the linear part domain that we have tested (see Fig. 6).

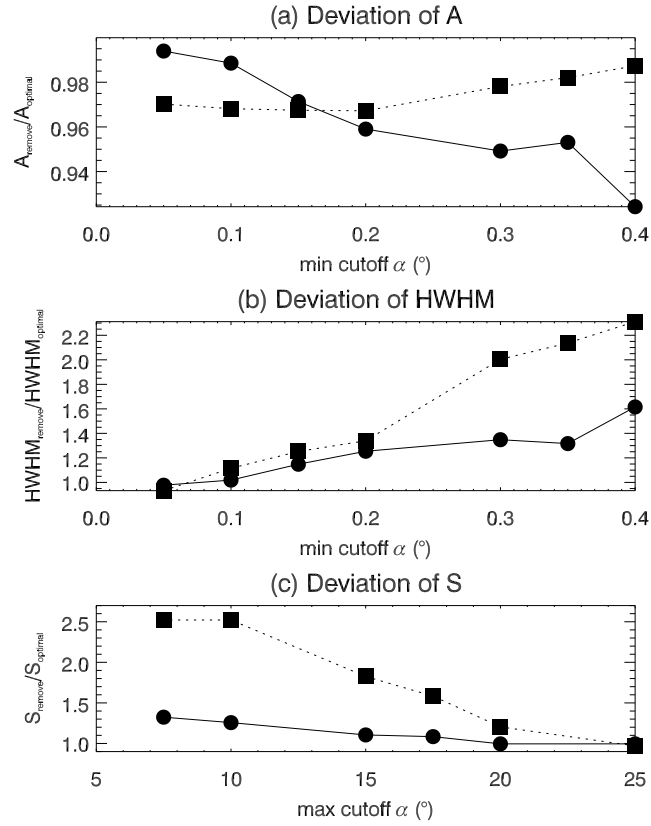


Fig. 6. Deviation of the linear-exponential model of Kaasalainen et al. (2001) for the morphological parameters A (a), HWHM (b) and S (c) when the phase angle coverage is incomplete. Circles and squares correspond to the cutoff of the incomplete phase functions of respectively the B ring and C ring typical phase curves (Fig. 5).

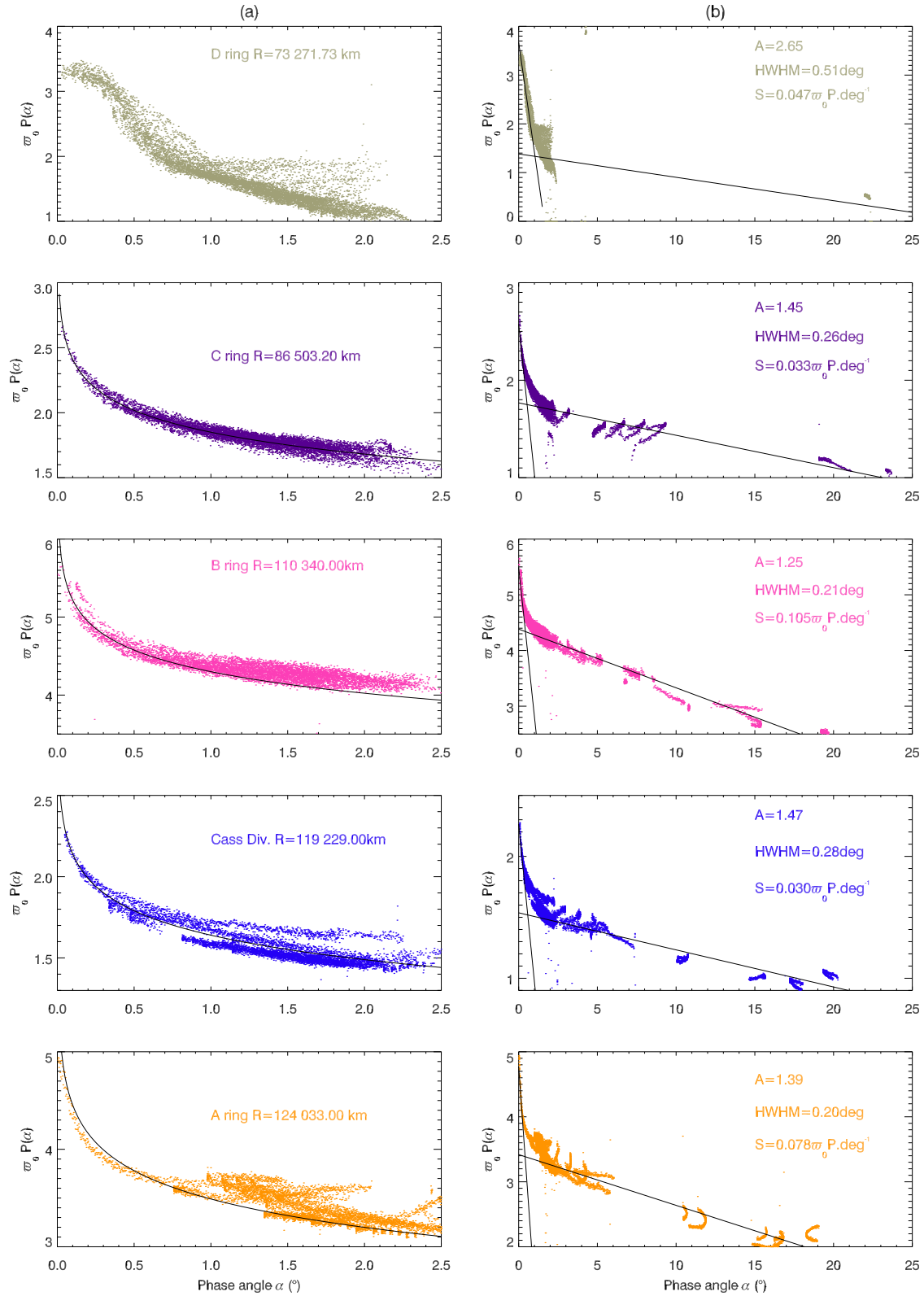


Fig. 7. Representative CLEAR phase curves for the main rings with a zoom on the surge (a) and the full phase curve (b), fitted respectively with the logarithmic model of Bobrov (1970) (a) and the linear-by-part model of Lumme and Irvine (1976) (b).

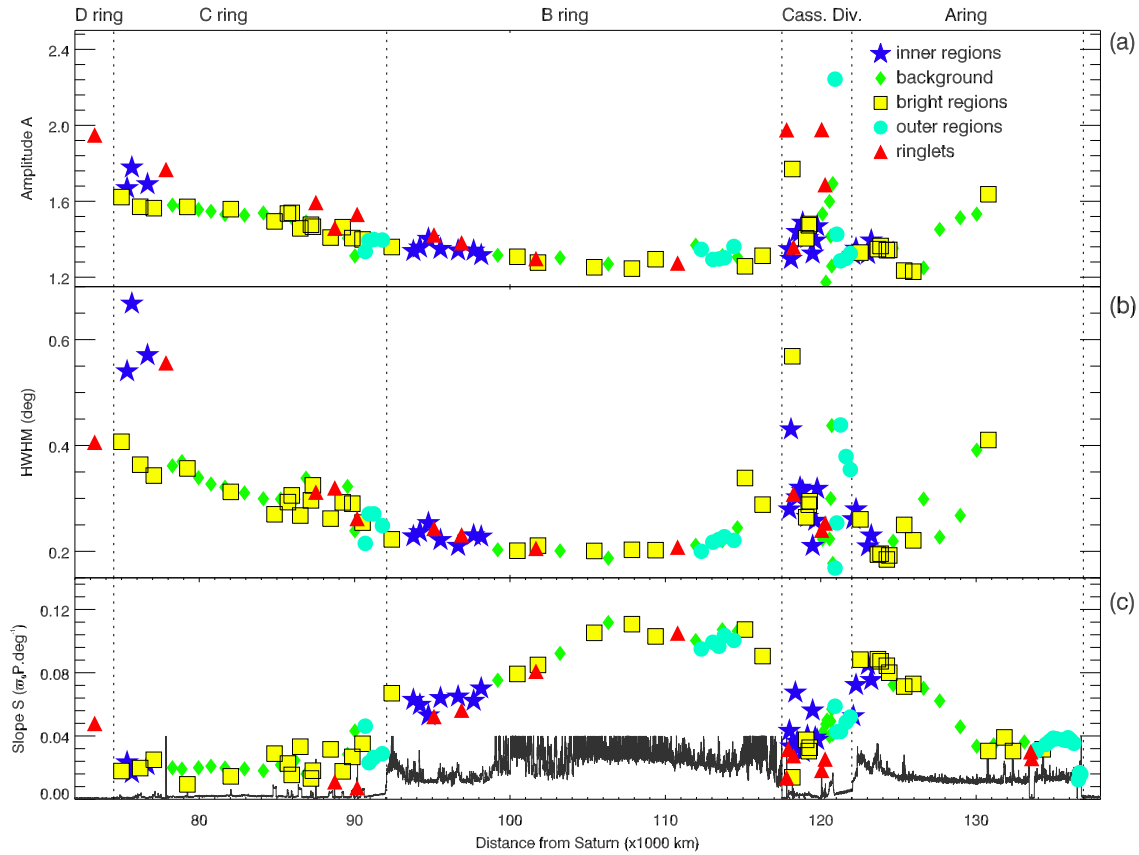


Fig. 8. Regional behavior of the morphological parameters : (a) the amplitude A , (b) the angular width HWHM in degrees and (c) the absolute slope S in $\varpi_0 P \cdot \text{deg}^{-1}$ from the Linear-by-part model of Lumme and Irvine (1976) for CLEAR phase curves using the ring type classification. The vertical dotted lines correspond to ring boundaries. The optical depth of PPS/Voyager is plotted in (c) as a radial reference.

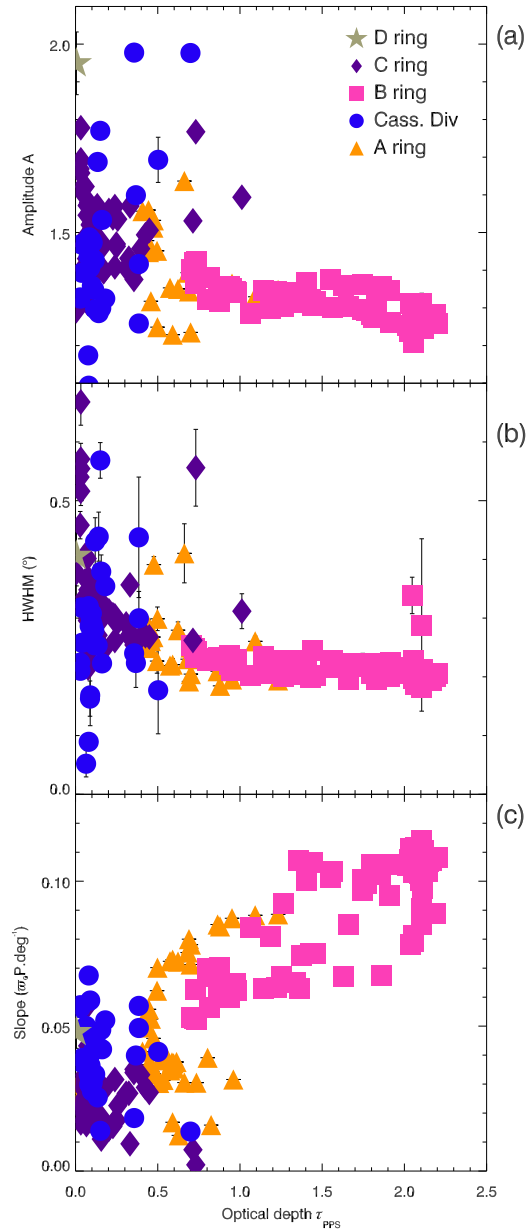


Fig. 9. Morphological parameters of CLEAR phase curves from the Linear-by-part model of Lumme and Irvine (1976) : Amplitude A (a), Angular width HWHM (b) and absolute slope S (c) in $\varpi_0 P.\text{deg}^{-1}$.

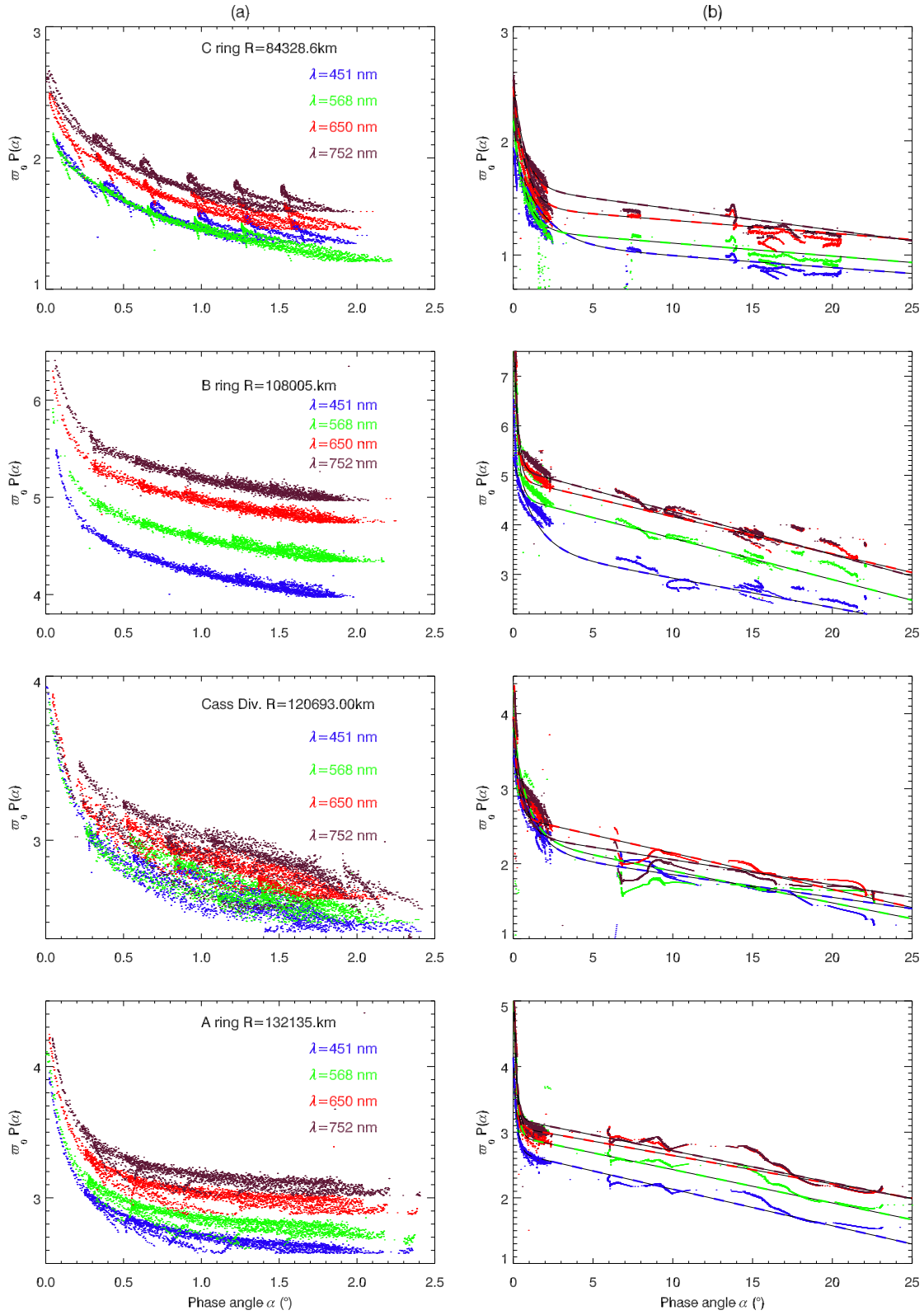


Fig. 10. Representative COLOR phase curves for the main rings with a zoom on the surge with WAC images (a) and the full phase curve with NAC and WAC images (b). Full phase curves of (b) are fitted with the linear-exponential model of Kaasalainen et al. (2001).

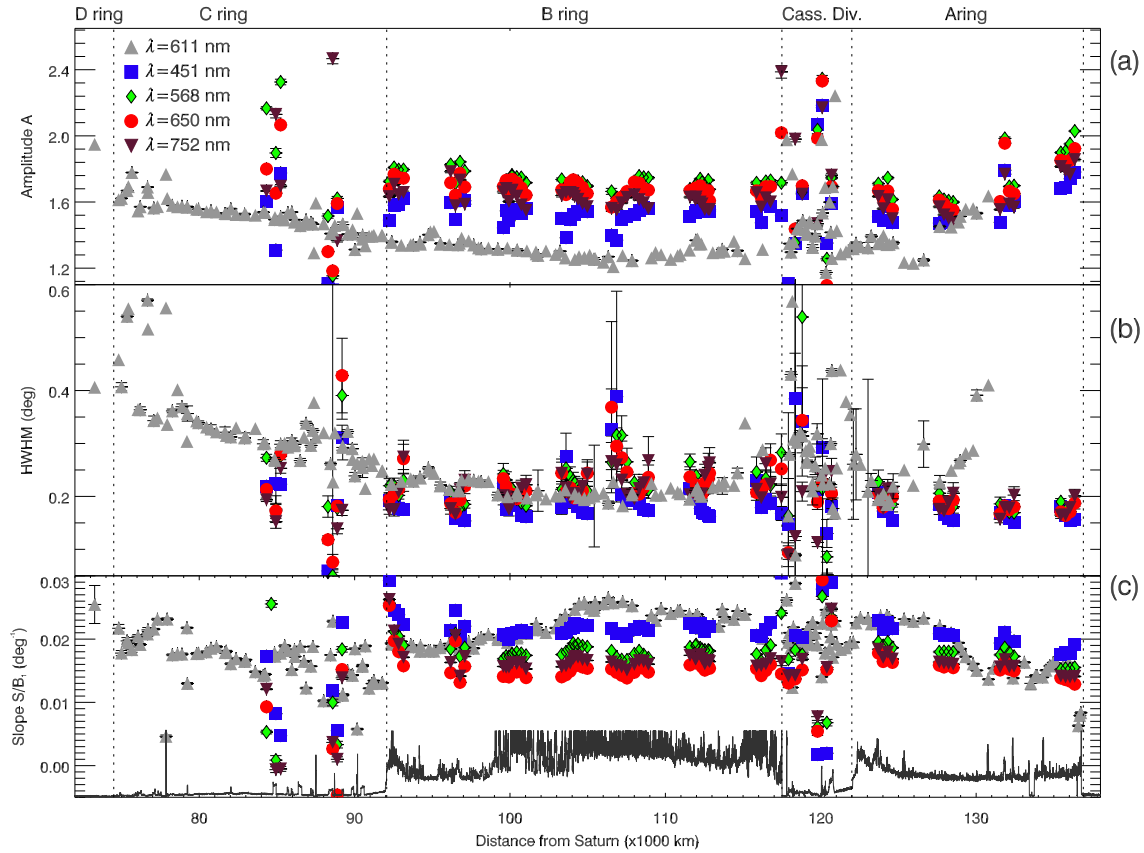


Fig. 11. Regional behavior of morphological parameters : (a) the amplitude A , (b) the angular width HWHM and (c) unitless absolute slope S/B_1 in deg^{-1} from the Linear-by-part model of Lumme and Irvine (1976) using CLEAR and COLOR phase curves. The vertical dotted lines correspond to ring boundaries. The optical depth of PPS/Voyager is plotted in (c) as a radial reference.

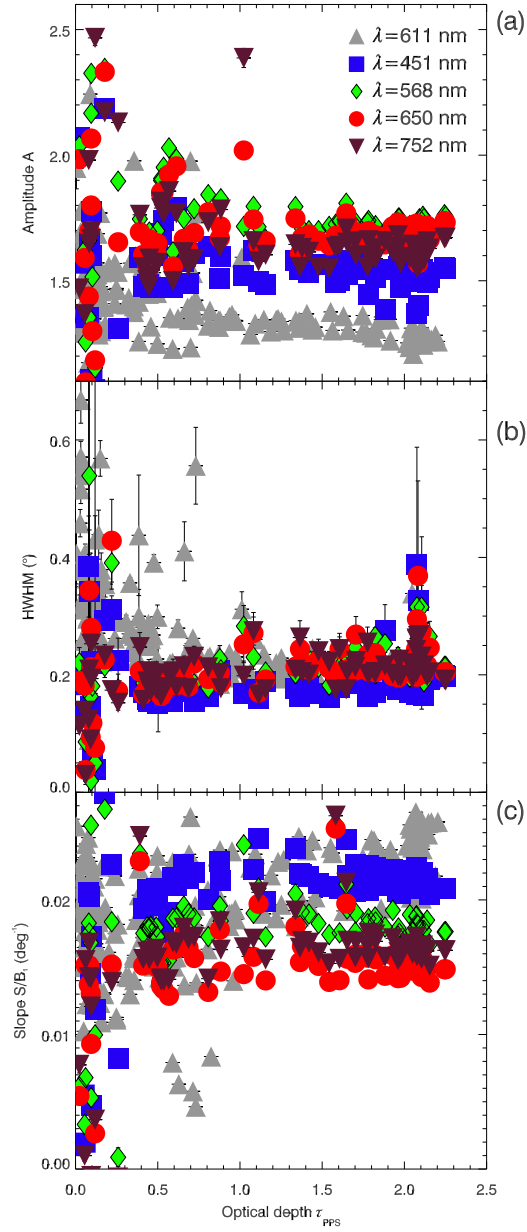


Fig. 12. Morphological parameters of CLEAR and COLOR phase curves from the Linear-by-part model of Lumme and Irvine (1976) : (a) the amplitude A , (b) the angular width HWHM and (c) the unitless absolute slope S/B_1 in deg^{-1} .

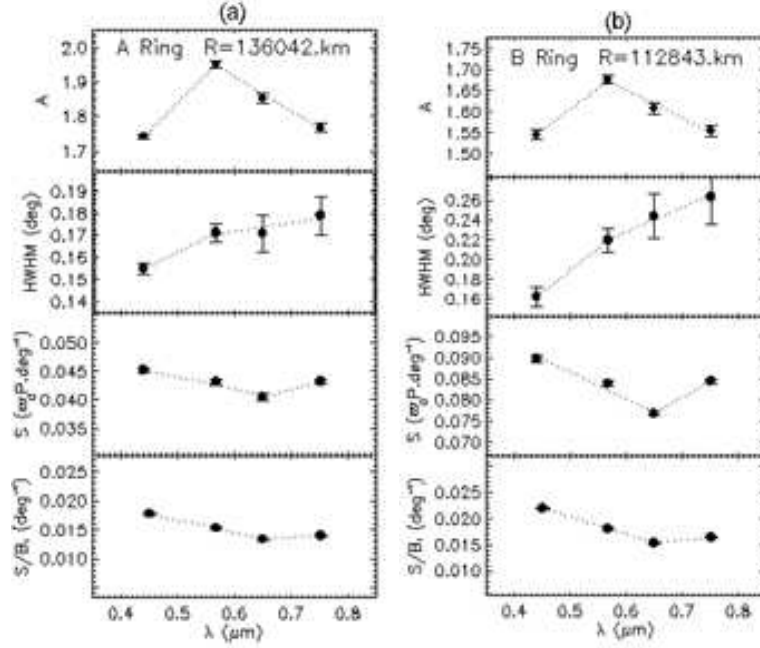


Fig. 13. Variations of the morphological parameters $A(\lambda)$, $\text{HWHM}(\lambda)$, the absolute slope $S(\lambda)$ and the unitless absolute slope $S/B_1(\lambda)$ for two typical regions of the A ring (a) and in the B ring (b). Dotted lines correspond to linear fits obtained in the spectral ranges. The slopes of these linear functions are called “steepness” and are correlated with the rings’ optical depth in tables 4 and 5.

Electronic supplementary material

Table 1: Outputs of the logarithmic model of Bobrov (1970) for the CLEAR phase curves representing each ring types (*inner* corresponds to inner regions characterized by low optical depth, *background* are morphological smooth regions without abrupt variation of optical depth, *bright* corresponds to bright regions that have the highest optical depth in each ring, *ringlet* corresponds to a thinner ring embedded in a less dense region or a gap, and *outer* corresponds to outer regions that mark the transition at each ring boundary) of each main ring. Horizontal lines correspond to the ring boundaries. We give for each ring type, the normal optical depth of the Voyager/PPS instrument and the corresponding radius (the distance from Saturn’s center). $f_{\varpi_0 P \rightarrow I/F}$ is a conversion factor which corresponds to the mean level of I/F curves over the mean level of $\varpi_0 P$ curves.

Rad. (km)	τ_{PPS}	Ring type	a_0	a_1	$f_{\varpi_0 P \rightarrow I/F}$
73271.7	0.005	ringlet	2.023	-0.6457	0.00001
74996.2	0.058	bright	1.105	-0.2097	0.0223
75356.9	0.027	inner	1.331	-0.2857	0.1255
75665.0	0.032	inner	1.072	-0.2535	0.1232
76199.8	0.132	bright	1.128	-0.1899	0.1255
76671.2	0.031	inner	1.188	-0.2561	0.1253
77075.4	0.119	bright	1.263	-0.2106	0.0643
77862.3	0.731	ringlet	0.568	-0.1074	0.0488
78273.0	0.079	background	1.242	-0.2130	0.0501
78889.1	0.074	background	1.182	-0.2030	0.0545
79238.2	0.331	bright	0.807	-0.1237	0.0310
79956.9	0.096	background	1.217	-0.1985	0.1189
80757.8	0.109	background	1.213	-0.1962	0.1259
table continues on next page...					

Rad. (km)	τ_{PPS}	Ring type	a_0	a_1	$f_{\varpi_0 P \rightarrow I/F}$
81661.4	0.117	background	1.186	-0.1845	0.0466
82031.0	0.202	bright	0.969	-0.1540	0.0539
82914.0	0.133	background	1.242	-0.1907	0.0621
84125.6	0.102	background	1.352	-0.2052	0.0557
84844.4	0.425	bright	1.707	-0.2325	0.0418
85234.6	0.099	background	1.290	-0.1953	0.0432
85706.9	0.256	bright	1.335	-0.1978	0.1254
85953.3	0.227	bright	1.098	-0.1625	0.1252
86158.7	0.075	background	1.506	-0.2179	0.1249
86503.2	0.396	bright	1.853	-0.2430	0.1250
86877.4	0.066	background	1.404	-0.1984	0.0522
87189.3	0.153	bright	0.892	-0.1213	0.0430
87312.8	0.163	bright	1.019	-0.1440	0.1140
87506.6	1.011	ringlet	0.645	-0.0566	0.1163
88451.6	0.239	bright	1.869	-0.2257	0.1241
88725.6	0.156	ringlet	1.087	-0.1390	0.1223
89233.7	0.248	bright	1.695	-0.2038	0.1221
89547.1	0.045	background	1.995	-0.2505	0.1232
89851.1	0.307	bright	1.970	-0.2265	0.1233
90019.4	0.073	background	2.361	-0.2384	0.0687
90163.1	0.713	ringlet	1.373	-0.1719	0.0633
90509.7	0.355	bright	2.310	-0.2514	0.0895
90685.9	0.076	outer	2.454	-0.2532	0.1144
90929.2	0.099	outer	1.981	-0.2161	0.0985
91237.3	0.137	outer	2.060	-0.2253	0.1128
table continues on next page...					

Rad. (km)	τ_{PPS}	Ring type	a_0	a_1	$f_{\varpi_0 P \rightarrow I/F}$
91788.6	0.170	outer	2.276	-0.2447	0.0857
92390.9	1.629	bright	3.548	-0.3668	0.0952
93781.3	1.359	inner	3.398	-0.3418	0.1254
94201.6	0.935	inner	3.377	-0.3479	0.1256
94751.3	0.706	inner	3.010	-0.3528	0.1253
95107.0	0.732	ringlet	2.984	-0.3582	0.1249
95527.3	0.936	inner	3.421	-0.3460	0.1252
96659.0	1.340	inner	3.637	-0.3472	0.0542
96885.4	0.817	ringlet	3.213	-0.3492	0.0608
97661.4	0.976	inner	3.413	-0.3394	0.1265
98146.4	0.872	inner	3.497	-0.3387	0.1264
99213.5	1.458	background	3.721	-0.3418	0.1259
100475.	2.057	bright	3.882	-0.3486	0.1281
101671.	1.188	ringlet	3.698	-0.3279	0.0057
101800.	2.104	bright	3.939	-0.3401	0.1259
103223.	1.266	background	3.975	-0.3634	0.1236
105422.	2.070	bright	4.149	-0.3446	0.0818
106327.	2.069	background	4.139	-0.3577	0.0477
107847.	2.116	bright	4.302	-0.3634	0.0679
109367.	2.053	bright	4.428	-0.4181	0.1249
110789.	1.815	ringlet	4.250	-0.4146	0.1251
111953.	1.407	background	4.292	-0.4617	0.0766
112309.	1.910	outer	4.412	-0.4370	0.1249
113053.	1.768	outer	4.441	-0.4350	0.1253
113441.	1.744	outer	4.393	-0.4334	0.1263
table continues on next page...					

Rad. (km)	τ_{PPS}	Ring type	a_0	a_1	$f_{\varpi_0 P \rightarrow I/F}$
113667.	1.358	background	4.306	-0.4675	0.1269
113796.	1.563	outer	4.394	-0.4632	0.1261
114411.	1.746	outer	4.344	-0.4653	0.1262
114637.	1.440	background	4.342	-0.4818	0.1266
115122.	2.047	bright	4.506	-0.5140	0.1268
116254.	2.105	bright	4.547	-0.4917	0.1249
117803.	0.698	ringlet	0.722	-0.2112	0.1265
117910.	0.087	ringlet	1.506	-0.0942	0.1266
117983.	0.113	inner	2.119	-0.2572	0.1272
118084.	0.119	inner	1.883	-0.2250	0.1269
118168.	0.150	bright	1.329	-0.2249	0.1288
118241.	0.099	ringlet	1.324	-0.1754	0.0204
118365.	0.080	inner	2.172	-0.1818	0.0222
118482.	0.091	inner	1.960	-0.2528	0.0464
118668.	0.079	inner	1.897	-0.2426	0.0225
118836.	0.083	inner	1.718	-0.2306	0.0475
119061.	0.082	bright	1.878	-0.2338	0.0435
119145.	0.089	inner	1.958	-0.2494	0.1003
119229.	0.104	bright	1.640	-0.2175	0.0508
119285.	0.097	bright	1.824	-0.2418	0.0561
119476.	0.029	inner	2.604	-0.3045	0.0626
119644.	0.038	inner	1.986	-0.2493	0.0527
119768.	0.032	inner	2.186	-0.2975	0.0639
120060.	0.356	ringlet	1.509	-0.2411	0.0518
120116.	0.161	background	1.939	-0.2629	0.0560
table continues on next page...					

Rad. (km)	τ_{PPS}	Ring type	a_0	a_1	$f_{\varpi_0 P \rightarrow I/F}$
120279.	0.134	ringlet	1.600	-0.2347	0.1158
120335.	0.077	background	1.980	-0.2603	0.0448
120408.	0.064	background	2.168	-0.2863	0.0423
120565.	0.367	background	2.328	-0.3048	0.0370
120638.	0.385	background	2.574	-0.3377	0.0051
120711.	0.384	background	2.625	-0.3319	0.0326
120773.	0.502	background	2.621	-0.3319	0.0465
120918.	0.089	outer	2.637	-0.3581	0.0952
121031.	0.116	outer	2.318	-0.2747	0.1058
121272.	0.140	outer	2.427	-0.2736	0.1093
121626.	0.156	outer	2.685	-0.2951	0.0563
121901.	0.180	outer	2.786	-0.3296	0.0790
122097.	0.458	inner	2.887	-0.3562	0.1254
122269.	0.623	inner	3.366	-0.4469	0.1253
122553.	1.092	bright	3.862	-0.4958	0.1247
123040.	0.864	inner	3.696	-0.4431	0.1254
123249.	0.681	inner	3.478	-0.4386	0.1235
123676.	1.231	bright	3.911	-0.4554	0.1254
123848.	0.951	bright	3.731	-0.4466	0.1251
124252.	0.878	bright	3.576	-0.4149	0.1238
124409.	0.690	bright	3.451	-0.4045	0.1246
124659.	0.574	background	3.305	-0.3920	0.1245
125367.	0.699	bright	3.075	-0.3468	0.1256
125951.	0.590	bright	3.212	-0.3655	0.1256
126619.	0.498	background	3.074	-0.3872	0.1256
table continues on next page...					

Rad. (km)	τ_{PPS}	Ring type	a_0	a_1	$f_{\varpi_0 P \rightarrow I/F}$
127655.	0.495	background	2.929	-0.3742	0.1257
128977.	0.473	background	2.694	-0.3465	0.1256
130037.	0.476	background	2.568	-0.3344	0.1254
130786.	0.661	bright	2.637	-0.3575	0.1254
131122.	0.465	background	2.556	-0.3406	0.1254
131818.	0.803	bright	2.764	-0.3932	0.1253
132372.	0.735	bright	2.478	-0.3015	0.1253
133105.	0.463	background	2.438	-0.3082	0.1253
133513.	0.012	ringlet	3.354	-1.0378	0.1253
133574.	0.027	ringlet	1.028	-0.3205	0.1251
133820.	0.509	outer	2.196	-0.1977	0.1250
133917.	0.534	outer	2.375	-0.2581	0.1250
134280.	0.959	bright	2.390	-0.2465	0.1249
134493.	0.575	outer	2.435	-0.2647	0.1249
134737.	0.585	outer	2.440	-0.2657	0.1247
134965.	0.558	outer	2.429	-0.2550	0.1246
135166.	0.548	outer	2.340	-0.2079	0.1245
135595.	0.614	outer	2.282	-0.1600	0.1247
135808.	0.596	outer	2.232	-0.1423	0.1246
135913.	0.523	outer	2.263	-0.1494	0.0234
136070.	0.586	outer	2.194	-0.1160	0.0526
136288.	0.602	outer	2.154	-0.0992	0.1254
136579.	0.627	outer	1.795	-0.0080	0.1216
136665.	0.590	outer	1.963	-0.0159	0.1206
136736.	0.824	outer	1.714	-0.0040	0.1198
table continues on next page...					

Rad. (km)	τ_{PPS}	Ring type	a_0	a_1	$f_{\varpi_0 P \rightarrow I/F}$
140338.	0.065	ringlet	0.240	-0.0090	0.1214